Five decades observing Earth's atmospheric trace gases using ultraviolet and visible backscatter solar radiation from space

Gonzalo Gonzalez Abad [a],[*], Amir Hossein Souri [a], Juseon Bak [a], Kelly Chance [a], Lawrence E. Flynn [b], Nickolay A. Krotkov [c], Lok Lamsal [c], Can Li [c],[d], Xiong Liu [a], Christopher Chan Miller [a], Caroline R. Nowlan [a], Raid Suleiman [a], Huiqun Wang [a]

[a] Harvard-Smithsonian Center for Astrophysics, 60 Garden Street, Cambridge, MA 02138, USA
[b] NOAA, College Park, MD 20740, USA
[c] NASA Goddard Space Flight Center, Greenbelt, MD 20771, USA
[d] Earth System Science Interdisciplinary Center, University of Maryland, College Park, MD 20742, USA

ARTICLE INFO

ABSTRACT

Over the last five decades, Earth's atmosphere has been extensively monitored from space using different spectral ranges. Early efforts were directed at improving weather forecasts with the first meteorological satellites launched in the 1960s. Soon thereafter, the intersection between weather, climate and atmospheric chemistry led to the observation of atmospheric composition from space. During the 1970s the Nimbus satellite program started regular monitoring of ozone integrated columns and water vapor profiles using the Backscatter Ultraviolet Spectrometer, the Infrared Interferometer Spectrometer and the Satellite Infrared Spectrometer instruments. Five decades after these pioneer efforts, continuous progress in instrument design, and retrieval techniques allow researchers to monitor tropospheric concentrations of a wide range of species with implications for air quality, climate and weather.

The time line of historic, present and future space-borne instruments measuring ultraviolet and visible backscattered solar radiation designed to quantify atmospheric trace gases is presented. We describe the instruments technological evolution and the basic concepts of retrieval theory. We include a review of algorithms developed for ozone, nitrogen dioxide, sulfur dioxide, formaldehyde, bromine monoxide, water vapor and glyoxal, a selection of studies using these algorithms, the challenges they face and how these challenges can be addressed. The paper ends by providing insights on the opportunities that new instruments will bring to the atmospheric chemistry, weather and air quality communities and how to address the pressing need for long-term, inter-calibrated data records necessary to monitor the response of the atmosphere to rapidly changing ecosystems.

Published by Elsevier Ltd.

1. Introduction

Since 1959 there have been 209 space missions devoted to the observation of the Earth's atmosphere [72]. The sensors used in these missions can be classified into two categories depending on the origin of the measured radiation. Passive instruments detect radiation generated by the Sun, the Earth and its atmosphere while active instruments use radiation generated artificially. A second classification depends on the observation geometry employed by the instrument. Nadir instruments point directly at the Earth's surface while limb instruments point at the edge of the atmosphere and take measurements at different tangent heights. Occultation instruments like ACE-FTS [13] use a limb geometry to point directly at the Sun or other stars.

Nadir observations probing the atmospheric column are sensitive to the boundary layer when using light at UV–vis wavelengths. Limb geometries have difficulties sampling the lower layers of the atmosphere but they can provide profile information at vertical resolution unavailable in the nadir geometry. Solar occultation instruments add excellent SNRs to the vertical profiling capability. This diversity of instruments and geometries provides information about a wide range of geophysical variables including temperature, pressure, winds, trace gas concentrations, aerosols and clouds.

The launch of the BUV [141] and TOMS [107] instruments in the 1970s marked the beginning of a new era for the study of the global distribution of atmospheric ozone (O_3). Since those early

[*] Corresponding author.
E-mail address: ggonzalezabad@cfa.harvard.edu (G. Gonzalez Abad).

days, steady progress in instrument capabilities (e.g., increased SNR, spectral coverage and spatial resolution) and algorithm development have extended the sensitivity of these instruments from the stratosphere and upper troposphere to the lower atmosphere. In 1995, ESA launched the ERS-2 satellite carrying GOME [31,76], now known as GOME-1, as part of its payload. GOME-1 UV–vis sensors provided valuable data for studying not only the stratospheric O_3 layer, but also tropospheric chemistry and pollution on a global scale.

Today, UV–vis observations from space provide significant insights into air quality and atmospheric chemistry. Satellite global observations are essential contributions to global observing systems [8]. For example, the oxidation capacity of the troposphere is directly linked to O_3 concentration [155]. The tropospheric O_3 concentration depends on natural (e.g., transport of stratospheric O_3 to the troposphere and photochemical production derived from biogenic precursors) and anthropogenic factors (e.g., photochemical production derived from precursors generated by human activities) [84] that can be detected using satellite sensors [e.g., 165]. Moreover, O_3 photochemical production can be constrained globally using satellite observations [293]. The combination of nitrogen dioxide (NO_2), sulfur dioxide (SO_2), formaldehyde (H_2CO) and glyoxal ($C_2H_2O_2$) observations can constrain the chemical regime of O_3 production and help determine the impact of human activities, informing air quality manager decisions [70]. Furthermore, satellites can also contribute to the understanding of the role of halogen chemistry in tropospheric chemistry and stratospheric O_3 [235]. Global satellite retrievals of bromine monoxide (BrO), iodine monoxide (IO) and chlorine dioxide (OClO) are helping researchers understand the effects of halogens in remote areas on a global scale.

A series of publications in the latter part of the first decade of the 2000s summarized the state of the field at that time and provided insights of the challenges laying ahead [30,44,84,178]. One decade later, steady progress has resulted in a new generation of instruments with enhanced capabilities. Some of these instruments are already orbiting the Earth, others like the constellation of geostationary air quality instruments, are planned to be launched in the near future. Besides instrument development, the last decade has seen significant progress on retrieval algorithms, exploitation of satellite data in scientific studies (e.g., inversions and data assimilation) and validation of satellite measurements using in-situ and remote sensing fiducial measurements.

This paper aims to provide a review of historic, present and future nadir viewing instruments measuring solar UV–vis backscattered radiation and examine how these missions have contributed to the understanding of reactive atmospheric trace gases and the complexity of air quality modelling. We include sections on O_3, NO_2, SO_2, H_2CO, BrO, H_2O and $C_2H_2O_2$, providing a comprehensive list of the retrievals produced for each molecule and some of their more significant applications. Discussions on aerosol retrievals derived from space-based UV–vis instruments are beyond the selected scope of this paper despite being a relevant component of air quality observing systems. Likewise, carbon monoxide is excluded as it is observed using infrared radiation.

Section 2 provides a historic review describing the evolution of instruments and technological advancements that have resulted in current observational capabilities. Section 3 focuses on the techniques used to exploit UV–vis observations and retrieve trace gas concentrations. Section 4 summarizes UV–vis space observations of O_3, NO_2, SO_2, H_2CO, BrO, H_2O, and $C_2H_2O_2$ including scientific studies, applications, limitations and challenges of these datasets. Section 5 presents our conclusions and a series of recommendations for the future. Table 1 provides the definition of most acronyms and abbreviations used in the text.

2. Past, present and future space-borne UV–vis instruments

Early efforts to analyze atmospheric composition using remote sensing date back to the nineteenth century. Samuel P. Langley invented the bolometer [151] to obtain precise measurements of the infrared through the near UV Sun radiation in order to determine the mean value of the solar constant and its variations. To fully exploit the capabilities of the new instrument, Langley and Abbot developed substantial new experimental techniques (such as an early chart recorder) and various analysis techniques (e.g., the "Langley plot", introducing the air mass factor concept), including photographic techniques for high pass filtering to produce line spectra from "bolographs", foreshadowing the high pass filtering used today by researchers employing the Differential Optical Absorption Spectroscopy (DOAS) technique for analyzing atmospheric spectra [152].

Fabry and Buisson [77,78] not only studied the coefficients of O_3 absorption they also conducted the first measurements of atmospheric O_3 by analyzing its absorption signatures at different wavelengths in direct sunlight observations using photographic spectographs. Gordon Dobson designed in 1927 a photoelectric spectrometer with the objective of measuring total atmospheric O_3 [68] using direct observations of the Sun. The Dobson spectrometer measures solar radiation at two suitable wavelengths (305 nm and 325 nm) to work out their ratio in order to calculate the amount of O_3. Using the same type of instrument the vertical distribution of O_3 can be estimated. The "Umkehr" method, proposed by Götz et al. [99], relies on pointing the spectrometer towards zenith to measure the intensity of scattered radiation at different altitudes. Making measurements at two different wavelengths for a set of solar zenith angles it is possible to deduce the vertical distribution of O_3. These pioneering works share similar concepts with modern ground-based and space-borne instruments. Despite decades of technological advances and theoretical studies the basic physical principles behind these works are similar to the ones supporting current ground-based and space-borne instruments.

The first space-based measurements of atmospheric O_3 using UV radiance were obtained with instruments designed to study the ionosphere and the mesosphere at wavelengths shorter than 300 nm [123,134,216]. Due to Rayleigh scattering and strong O_3 absorption, the penetration of photons below 300 nm is limited to the highest layers of the troposphere.

The BUV instrument on-board Nimbus-4 initiated the era of satellite instruments specifically designed to study atmospheric composition using UV backscatter solar radiance in 1970. By including spectral measurements up to 340 nm, this instrument was suitable for observations of total column O_3 with enhanced stratospheric and tropospheric sensitivity [108]. Over the next three decades, follow up instruments SBUV [86,87], SBUV/2 [64] and TOMS [107] extended and consolidated the lessons learned from BUV and improved its spatial and spectral resolution. BUV and SBUV instruments measured twelve 1 nm wide bands ranging from 255 nm to 340 nm at direct nadir only. TOMS only measured six 1 nm bands from 312 nm to 380 nm. However, it was equipped with a cross-track scanning capability that allowed daily global observations at a resolution of 50×50 km^2 for the first time. These early instruments used a single PMT detector, preserving the accuracy of radiometric measurements across different wavelength bands. SBUV sensors were also capable of measuring in continuous scan mode, recording spectra from 160 nm to 400 nm at 1 nm FWHM resolution and 0.14 nm sampling, with reduced temporal and spatial resolution.

The SBUV continuous mode was improved with GOME-1 [76], launched in 1995 on-board ESA's ERS-2 satellite, initiating the era of hyperspectral UV–vis spectrometers. The GOME-1 innovative design consisted of a double monochromator combining a predis-

Table 1

List of acronyms.

ACE-FTS	Atmospheric Chemistry Experiment-Fourier Transform Spectrometer
AERONET	AErosol RObotic NETwork
ADEOS	Advanced Earth Observing Satellite
AMSRE	Advanced Microwave Scanning Radiometer for EOS
ARM	Atmospheric Radiation Measurement
BUV	Backscatter UltraViolet
CCD	Charge Coupled Device
CMA	China Meteorological Administration
CNSA	China National Space Agency
COSMIC	Constellation Observing System for Meteorology, Ionosphere and Climate
CTM	Chemical Transport Model
DSCOVR	Deep Space Climate Observatory
ECV	Essential Climate Variable
EMI	Environmental Monitoring Instrument
EnviSat	Environmental Satellite
EPIC	Earth Polychromatic Imaging Camera
EOS	Earth Observing System
ERS-2	European Remote Sensing-2
ESA	European Space Agency
EUMETSAT	European Organisation for the Exploitation of Meteorological Satellites
FWHM	Full Width at Half Maximum
GCOS	Global Climate Observing System
GEMS	Geostationary Environment Monitoring Spectrometer
GEO	Geosynchronous Equatorial Orbit
GEOS-Chem	Goddard Earth Observing System-Chemistry
GEWEX	Global Energy and Water cycle EXchanges
GF-5	Gao Fen-5
GNSS	Global Navigation Satellite System
GOME(-1)	(first) Global Ozone Monitoring Experiment
GOME-2	Global Ozone Monitoring Experiment-2
GPS	Global Positioning System
GRUAN	GCOS Reference Upper-Air Network
LEO	Low Earth Orbit
MEaSUREs	Making Earth System Data Records for Use in Research Environments
NASA	National Aeronautics and Space Administration
NCAR	National Center for Atmospheric Research
NIVR	Nederlands Instituut voor Vliegtuigontwikkeling en Ruimtevaart
NMVOC	Non Methane Volatile Organic Compound
NOAA	National Oceanic and Atmospheric Administration
OCO-2	Orbiting Carbon Observatory-2
OMI	Ozone Monitoring Instrument
OMPS	Ozone Mapping and Profiler Suite
OMPS-NM	OMPS-Nadir Mapper
OMPS-NP	OMPS-Nadir Profiler
OSIRIS	Optical Spectrograph and InfraRed Imager System
PDA	PhotoDiode Array
PMT	PhotoMultiplier Tube
QA4ECV	Quality Assurance for Essential Climate Variables
RTM	Radiative Transfer Model
SBUS	Solar Backscatter Ultraviolet Sounder
SBUV	Solar Backscatter UltraViolet
SCIAMACHY	SCanning Imaging Absorption SpectroMeter for Atmospheric CHartographY
S-NPP	Suomi National Polar-orbiting Partnership
SNR	Signal to Noise Ratio
SSMI	Special Sensor Microwave Imager
SSMIS	Special Sensor Microwave Imager/Sounder
S5	Sentinel 5
S5P	Sentinel 5 Precursor
SZA	Solar Zenith Angle
TEMPO	Tropospheric Emissions: Monitorig of POllution
TOMS	Total Ozone Monitoring Spectrometer
TOMS-EP	TOMS-Earth Probe
TOU	Total Ozone Unit
TROPOMI	TROPOspheric Monitoring Instrument
UV	UltraViolet
VIS	VISible
VOC	Volatile Organic Compound
VLIDORT	Vector LInearized Discrete Ordinate Radiative Transfer

perser prism and four grating spectrometers with linear PDAs, allowing the measurement of continuous spectra from 240 nm to 790 nm at resolutions of 0.22 nm to 0.40 nm. GOME-1 standard operation mode provided a spatial footprint of 40×320 km^2. This footprint combined with the scanning mechanism provided global coverage in three days. The spectral capabilities of GOME-1 were suitable for the development of retrievals beyond O_3 and SO_2 and started the era of air quality characterization from space. Exploiting the hyperspectral capabilities of the instrument, new retrievals of tropospheric O_3, NO_2, H_2CO, $C_2H_2O_2$, BrO, and H_2O

were developed. GOME-1 was proposed as a precursor of the SCIAMACHY [23] instrument launched in 2002 as part of ESA's EnviSat payload. SCIAMACHY had three operating modes: limb, occultation and nadir. In the nadir mode, SCIAMACHY provided higher spatial resolution and extended spectral coverage compared with GOME-1 to measure CH_4, CO and CO_2 using short-wave infrared.

The next ground breaking technological advancement happened in 2004 with the launch of OMI. The linear PDA detectors of the GOME-1 and SCIAMACHY instruments were replaced by 2-dimensional CCD detectors [158] following the success of the OSIRIS limb instrument [168]. This new design revolutionized monitoring of air quality from space. It allowed finer spatial resolution measurements while keeping spectral performance and eliminating the need for a scanning mechanism. This new concept, when used in LEO satellites, allows for wide swaths, with daily global coverage and high spatial resolution. Besides the technological innovation in the detectors, the remarkable stability of OMI's performance [157] and its enhanced spatial resolution has allowed for the first time the detection and quantification of point emitters [81], the characterization of urban scale chemical processes and to study the decadal evolution of air quality [70]. The GOME-1 and OMI instruments were followed by GOME-2 [195], OMPS-NM [229], OMPS-NP [207] and TROPOMI [260] instruments supported by ESA, EUMETSAT, NASA and NOAA. In recent years, China has developed its own air quality program relying on the SBUS [120], TOU [277] and EMI [292] instruments supported by the CMA and the CNSA. A comprehensive list of past and current instruments is provided in Table 2 including information about their fundamental characteristics.

The instruments described in Table 2 are payloads on spacecrafts in Sun-synchronous polar LEOs, measuring the sunlit part of the globe in the morning (9:00–11:00 local time (LT)) or early afternoon (12:00–14:30 LT). Among all past and currently operating satellite instruments, TROPOMI offers the highest spatial resolution (3.5×7 km^2) while OMI offers the longest record, and least instrument degradation [227]. The only exception to LEO orbit instruments in Table 2 is EPIC [177]. The DSCOVR spacecraft, with EPIC as payload, was launched on February 2015 reaching its first Lagrange point orbit on June 2015. From this orbit, EPIC scans Earth's sunlit full-disk with high spatial (18 km^2 at nadir) and temporal (almost hourly) resolutions. EPIC's ten spectral channels allow the retrieval of total column O_3 and volcanic SO_2.

To increase the number of observations over a particular location on a day, a new generation of space air quality instruments, to be deployed on GEO satellites, are being developed, building on the heritage of spectrometers flown in LEO. Three instruments are planned to be launched in the near future: Korea's Aerospace Research Institute GEMS [130] instrument will observe East Asia, NASA's TEMPO [303] will observe North America and ESA's Sentinel 4 (and planned follow up missions) [122] will observe Europe. These instruments will provide hourly measurements during the sunlit hours at unprecedented spatial resolutions as small as $\sim 2.5 \times 4.5$ km^2. To maximize the information obtained by these GEO instruments, given their expected geographical coverage, it is of paramount importance to combine them with LEO observations provided by GOME-2, TROPOMI and OMPS-NM instruments to produce inter-calibrated products. These products will allow near-real time monitoring of air quality and facilitate scientific studies at new spatial and temporal scales.

Along with the constellation of GEO instruments, air quality observations from LEO will continue in the next decades. The launch of Sentinel 5 (and follow up missions) starting in 2021 by ESA will provide morning observations while the afternoon overpass will be provided by OMPS-NM and OMPS-NP instruments to be launched by NOAA in several missions extending into the 2030s.

It is worth mentioning new initiatives in their early stages such us TROPOLITE, aiming to achieve a lighter version of TROPOMI [176] with enhanced spatial resolution (1×1 km^2), the Russian Ozonometer [66,67], the PanFTS instrument using Fourier Transform interferometry [225,284] and innovative designs using Fabry-Pérot interferometry [143].

3. Retrieval methods

After the incoming solar radiation enters the Earth's atmosphere, part of the radiation is absorbed by atmospheric trace gases and particles, part of the radiation is backscattered by air molecules, aerosols and clouds, and part of the radiation is reflected by Earth's surface. The top panel of Fig. 1 shows solar irradiance and Earth radiance measurements made by the GOME-1 instrument. The bottom panel, shows reflectance spectra derived for four different scenes. The distinct surface reflectance characteristics of clouds, oceans, deserts and vegetation determine the overall shape of the spectra. The interaction between light and trace gases absorption (e.g., shown in Fig. 2 top panel) leads to spectral signatures in the backscattered radiances as the ones shown in Fig. 1 bottom panel.

At wavelengths below 340 nm, atmospheric absorption is dominated by O_3 in the Hartely and Huggins bands. The mean photon path length, shown in Fig. 2 middle left panels, indicates that at shorter wavelengths (e.g., 250 nm), photons can only penetrate to ~ 40 km due to the strong O_3 absorption and Rayleigh scattering. With increasing wavelengths, O_3 absorption decreases by almost four orders of magnitude (from ~ 2 down to 10^{-4}) and Rayleigh scattering decreases proportionally to the fourth power of wavelength. In consequence more photons can penetrate deeper into the atmosphere. In the Huggins bands, a significant portion of photons can penetrate into the troposphere.

The wavelength-dependent O_3 absorption and Rayleigh scattering primarily provide information about the vertical distribution of the O_3 profile. The temperature dependent O_3 absorption in the Huggins bands further enhances sensitivity to tropospheric O_3 [50]. Similarly at longer wavelengths, the wide range of H_2O absorption might provide information about the H_2O profile. The wide range of O_2 absorption in the O_2–A band, and the noticeable O_2–O_2 absorption and their known concentrations can be used to derive aerosol and cloud vertical information. For most of the other trace gases, the absorption optical depth is typically on the order of 10^{-3} or smaller. Given their small optical depths, and the weak pressure and temperature dependence of their absorption features satellite measurements are mostly sensitive to their integrated vertical abundance.

The retrieval of trace gas concentrations from radiance measurements can be described as the inversion of Eq. (1). The goal is to estimate the values of a set of variables $\mathbf{x}$ (e.g., trace gas concentrations at different atmospheric levels, surface reflectance) given their relationship with a set of observations $\mathbf{y}$ (e.g., radiances at different wavelengths). The relationship between $\mathbf{x}$ and $\mathbf{y}$ is described by a forward model (i.e., a radiative transfer model, RTM) $\mathbf{F}$ depending on the state vector (retrieved) and a vector of model parameters $\mathbf{p}$ (not retrieved). Errors are expressed in Eq. (1) as $\boldsymbol{\epsilon}$.

$$\mathbf{y} = \mathbf{F}(\mathbf{x}, \mathbf{p}) + \boldsymbol{\epsilon} \tag{1}$$

Due to limitations in forward models and instrumentation as well as observation errors, $\boldsymbol{\epsilon}$ is never 0. For that reason the process of inverting Eq. (1) can only lead to a statistical estimate of $\mathbf{x}$, usually combining a-priori and observational information.

Below we briefly discuss the most common strategies employed to deal with the inversion problem and refer the reader to [221] for a detailed description of retrieval techniques. We also provide a

Table 2

Past and current nadir instruments using solar backscatter radiation for monitoring of atmospheric composition from LEO.

Instrument (Agency)	Satellite(s)	Operation period	ECT	Global coverage	Detector	Nominal pixel resolution [km^2]	Spectral range [nm]	Spectral resolution [nm]
BUV (NASA)	Nimbus-4	1970–1980	12:00 [a]	10 days	PMT	220	255.65 273.61 283.10 287.70 292.29 297.59 301.97 305.87 312.56 317.56 331.26 339.89	1
SBUV (NASA)	Nimbus-7	1979–1994	12:00[a]	14 days	PMT	200	As BUV	1
SBUV continous mode (NASA)	Nimbus-7	1979–1987	12:00[a]	N/A[d]	PMT	200	160–400	1
TOMS (NASA)	Nimbus-7/Meteor-3 TOMS-EP/ADEOS	1979–2006	12:00[a] N/A 10:30[a] 12:00[a]	1 day	PMT	50 (nadir)	312.5 317.5 331.3 339.9 360.0 380.0	1
SBUV/2 (NOAA)	NOAA-(9,11, 14,16,17,18,19)	1984[g]	12:00[a,c]	10 days	PMT	170	As BUV	1.1
GOME-1 (ESA)	ERS-2	1995–2011	10:30[a]	3 days	Linear PDA	40 × 320[e] 40 × 960[f]	240–790	0.22–0.40
SCIAMACHY nadir mode (ESA)	EnviSat	2002–2012	10:00[a]	6 days	Linear PDA	30 × 60[e] 30 × 120[f]	240–1750; 1934–2044 2259–2386	0.22–1.48
OMI (NASA/ESA/NIVR)	Aura	2004[g]	13:45[b]	1 day	2D CCD	13 × 24 (nadir)	270–500	0.42–0.63
GOME-2 (ESA/EUMETSAT)	Metop-(A/B/C)	2006[g]	9:30[a]	1.5 days	Linear PDA	40 × 80[e] 40 × 160[f]	240–790	0.24–0.53
SBUS (CMA)	FY-3(A/B/C)	2008[g]	9:05[a] 13.38[b] 10.15[a]	7 days	PMT	200	252.00 273.62 283.10 287.70 292.29 297.59 301.97 305.87 312.57 317.56 331.26 339.89	1
TOU (CMA)	FY-3(A/B/C)	2008[g]	9:05[a] 13.38[b] 10.15[a]	1 day	PMT	50 (nadir)	308.73 312.64 317.65 322.46 331.38 360.25	1
OMPS-NM (NASA/NOAA)	S-NPP NOAA-20	2011[g]	13.35[b]	1 day	2D CCD	50 (nadir) 17 (nadir)	300–380 297–420	1
OMPS-NP (NASA/NOAA)	S-NPP NOAA-20	2011[g]	13.35[b]	12 days	2D CCD	250	250–310	1
EPIC (NASA/NOAA)	DSCOVR	2015[g]	N/A	1 day	2D CCD	8 (nadir)	317.5, 325.0, 340.0, 388.0 443.0, 551.0, 680.0, 687.75 764.0, 779.5	0.84–3.0
TROPOMI (ESA)	S5P	2017[g]	13.30[b]	1 day	2D CCD	3.5 × 7 (nadir)	270–775 2305–2385	0.5–1 0.25
EMI (CNSA)	GF-5	2018[g]	13.30[b]	1 day	2D CCD	13 × 48 (nadir)	240–710	0.3–0.5

[a] Descending node.
[b] Ascending node.
[c] Orbits drift after 1–2 years [184].
[d] SBUV only operated in this mode 1 day per month.
[e] Forward scan.
[f] Backward scan.
[g] Still operational.

G. Gonzalez Abad, A.H. Souri and J. Bak et al./Journal of Quantitative Spectroscopy & Radiative Transfer 238 (2019) 106478

5

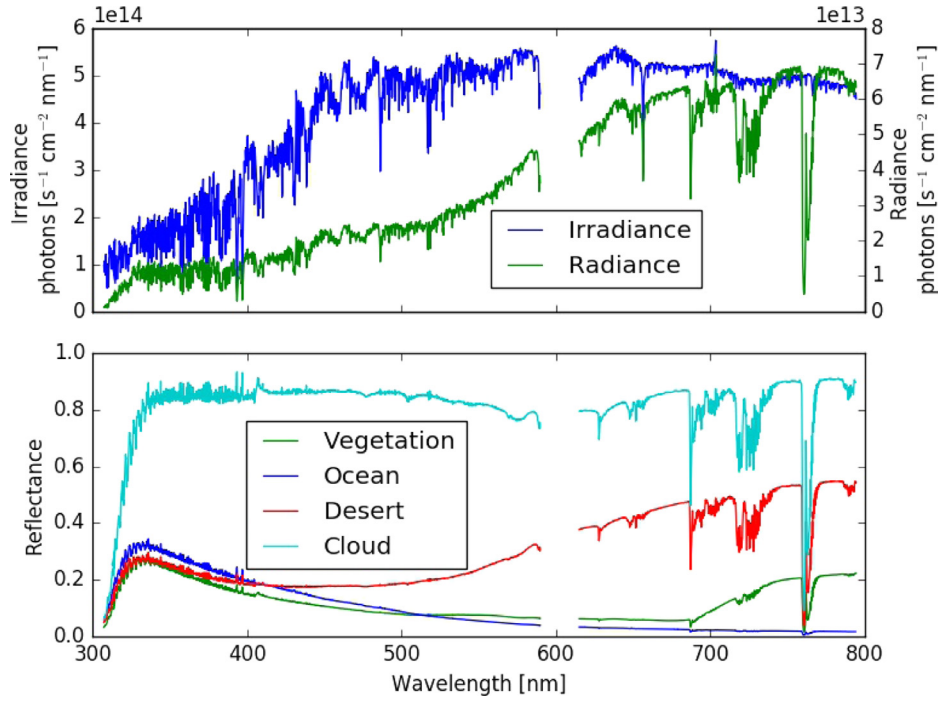**Fig. 1.** Upper panel shows two typical GOME-1 irradiance and radiance measurements. Lower panel shows the reflectance $[(\pi \times radiance)/(\cos(SZA) \times irradiance)]$ derived from GOME-1 measurements for different scenes in the UV–vis.

brief description of the algorithm physics needed to support modern retrieval techniques.

3.1. Optimal estimation

Optimal estimation (OE) [221] has become the standard for O_3 profile retrievals in the UV–vis. In the OE scheme the state vector $\mathbf{x}$ includes the O_3 profile, geophysical parameters (e.g., other trace gases, surface reflectance and cloud parameters) and other spectroscopic fit parameters (e.g., stray light, Ring effect patterns, and bandpass shape and spectral scale prescriptions). The measurement vector $\mathbf{y}$ is either the radiance or the ratio of the radiance to the irradiance, depending on the detailed approach.

The linearization of the forward model can be described as $\mathbf{x} = \mathbf{x}_a + \mathbf{K}^{-1}(\mathbf{y}\text{-}\mathbf{F}(\mathbf{x}_a))$ where $K_{i,j} = \partial F_i(\mathbf{x})/\partial x_j$ is the Jacobian or weighting function matrix with retrieved ($\mathbf{x}$) and a priori ($\mathbf{x}_a$) vectors respectively. Given the information content of the satellite observations this is often an ill-posed inversion problem. OE employs additional constraints so that a-priori information complements measurement constraint information. OE simultaneously minimizes the difference between measured and simulated radiances and the difference between retrieved and a priori states with relative weights determined by the Jacobian and the a priori and measurement covariance matrices. Because of non-linearity, the minimization of the cost function χ^2 (Eq. (2)) is iterated updating $\mathbf{x}$ to an a-posteriori solution (3) with $\mathbf{K}_i$ calculated for the latest completed iteration.

$$\chi^2 = \left\| \mathbf{S_y^{-\frac{1}{2}}} \{ \mathbf{K_i}(\mathbf{X_{i+1}} - \mathbf{X_i}) - [\mathbf{Y} - \mathbf{F}(\mathbf{X_i})] \} \right\|_2^2 + \left\| \mathbf{S_a^{-\frac{1}{2}}} (\mathbf{X_{i+1}} - \mathbf{X_a}) \right\|_2^2 \tag{2}$$

$$\mathbf{X_{i+1}} = \mathbf{X_i} + \left(\mathbf{K_i^T S_y^{-1} K_i} + \mathbf{S_a^{-1}} \right)^{-1} \left[\mathbf{K_i^T S_y^{-1}} (\mathbf{Y} - \mathbf{R}(\mathbf{X_i})) - \mathbf{S_a^{-1}} (\mathbf{X_i} - \mathbf{X_a}) \right] \tag{3}$$

where $\mathbf{X_i}$, $\mathbf{X_{i+1}}$, $\mathbf{X_a}$ are previous, current and a-priori state vectors, $\mathbf{Y}$, $\mathbf{F}$ are measured and simulated radiance vectors, $\mathbf{K}$ is the weight-

ing function matrix and $\mathbf{S_a}$, $\mathbf{S_y}$ the a-priori and measurement covariance matrices.

3.2. Discrete channel ozone retrievals

The Version 8 Total Column Ozone Algorithm (V8Toz) [280] is one of the newer versions of a long line of NASA algorithms designed to make efficient use of the sensitivity of the 317.5 vacuum nm channel to the total O_3 column and of the 331.3 vacuum nm channel to the surface and cloud reflectivity assuming that O_3 is the only absorber present in the Rayleigh atmosphere.

The algorithm uses RTM lookup tables (LUTs) to determine the geometric cloud fraction and effective reflectivity to explain the $\log_{10}$ (radiance/irradiance measurement ratio) called N-Value for the 331.3 nm channel. The LUT are dimensioned for total O_3 amounts populated with the radiative transfer results at 50 DU intervals for low, medium and high latitudes standard profiles. The table values, interpolated to geometric cloud fraction and viewing geometry are used to determine the total O_3 amount that explains the 317.5 nm N-Value measurement. The results from this first step are further refined using a set of climatological profiles [186] including information for each month at 10° latitude bands and temperature fields. A set of final empirical adjustments specific to atmospheric conditions is finally applied to the total O_3 value including the presence of UV-absorbing aerosols and profile shape sensitivity of the 313 nm channel at high optical path lengths.

The RTM LUTs contain information to provide measurement estimates for additional channels. The shorter wavelengths can be used to provide estimates of elevated atmospheric SO_2 amounts [287]. The total O_3 values derived in the second step are used to compute measurement residuals as relative differences between the measurements and the values for these additional channels.

The Version 8 Ozone Profile Retrieval Algorithm (V8Pro) [14] was developed to create an O_3 profile climate data record using the 12 channel measurements of the SBUV(/2) instruments [89] but is also used in the operational near-real-time SBUV/2 and OMPS retrievals at NOAA. As shown in Fig. 2, with increasing
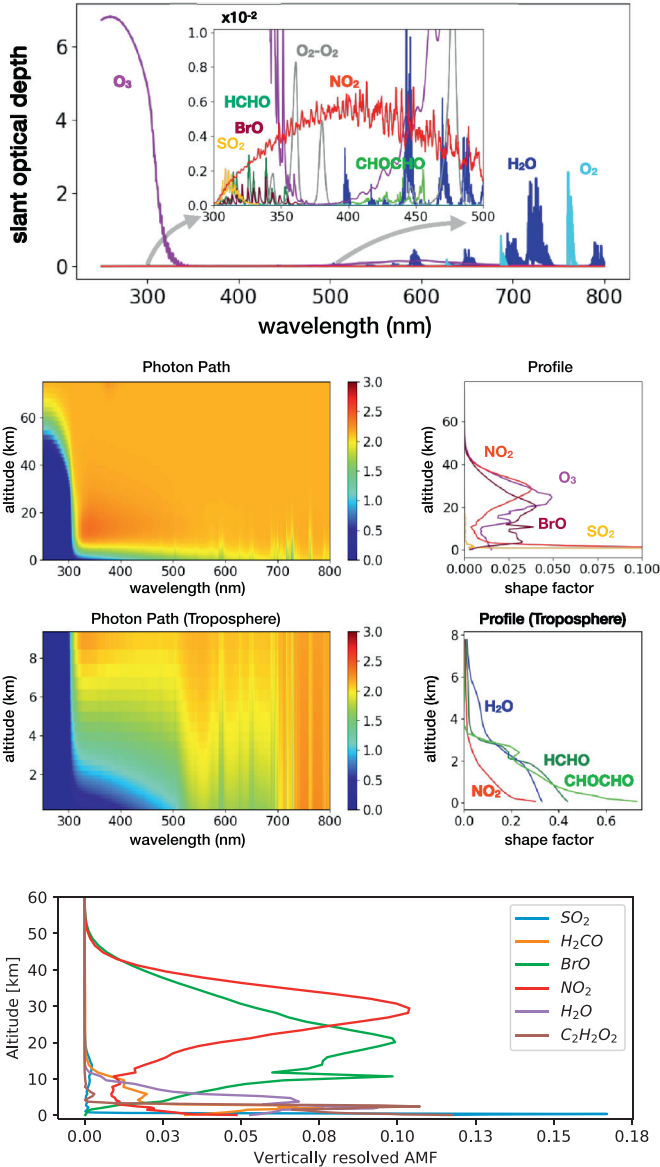
Fig. 2. Top panel: slant optical depths of the strongest absorbers. Middle left panels: simulated photon path detected by satellite sensors as functions of wavelength and altitude for 30° SZA, 0° VZA and homogeneous 0.1 surface reflectance. Simulations shown here were performed with the VLIDORT RTM for a Rayleigh atmosphere and molecular absorption from O_3, NO_2, O_2, O_2–O_2 and H_2O plus other minor species not relevant for the calculation of the photon paths. Middle right panels: shape factors for the different species assumed in the simulations. To enhance the spectral signatures of weak absorbers the simulations have considered high atmospheric loading of SO_2 and $C_2H_2O_2$. Bottom panel: vertically resolved AMFs computed at 326 nm (SO_2), 340 nm (H_2CO and BrO) and 440 nm (NO_2, H_2O and $C_2H_2O_2$).

wavelength from 250 nm to 320 nm, the O_3 absorption decreases and the photons penetrate more deeply into the atmosphere sampling different altitude regions. The wavelengths used in V8Pro were selected to give good coverage of the range of O_3 absorption cross sections present in the Hartley–Huggins bands with the absorption approximately doubling between adjacent wavelengths.

In this retrieval, **Y** is defined as the ten radiance/irradiance ratios (at [253, 273, 283, 288, 292, 298, 302, 306, 313, 318] nm) and **X** is a vector of 3 km layer O_3 amounts. The maximum likelihood retrieval is formulated using logarithms of **Y** as they show reduced nonlinear responses to O_3 profile changes. The measurement covariance matrix ($\mathbf{S_y}$) is a diagonal matrix of the relative noise for

each channel. The a-priori profile set and its covariance are derived from [186] climatology. Cloud and reflectivity information are obtained from the V8Toz algorithm described above. As explained in the OE section, the solution to this linearized approximation to the forward model is achieved using an iterative approach until the convergence criteria are meet.

3.3. Two step retrievals

Photon penetration above 330 nm (Fig. 2) varies weakly with increasing wavelengths limiting the information content of the hyperspectral satellite measurements. In this case, direct fitting is a suitable technique for the retrieval of slant column densities (SCDs) along the line of sight. A second step in these kind of retrievals implies the conversion of SCDs into vertical column densities (VCDs) using a-priori information and RTMs to calculate effective air mass factors (AMFs). This is the preferred approach to retrieve NO_2, SO_2, H_2CO, BrO, $C_2H_2O_2$ and H_2O VCDs.

The basis of this retrieval technique is to fit the high-pass filtered ratio of the Earth radiance and the solar irradiance, if the DOAS equation is to be used [211], the ratio of the radiance to the irradiance or simply directly fitting the radiance as described by [43] to laboratory-measured absorption cross-sections ($\tau(\lambda)$) of the target species and other interfering gases, a reference Ring spectrum (R(λ)) [50] and scaling and baseline polynomial functions (P_{sc} and P_{bl} respectively). The polynomials model the spectrally varying scattering effect of clouds and aerosols and reflection by the Earth's surface. Eq. (4) shows the model used in the case of direct fitting.

$$F(\lambda) = [I_0(\lambda)exp(-\tau(\lambda)) + R(\lambda)]P_{sc}(\lambda) + P_{bl}(\lambda) \qquad (4)$$

The source spectrum (I_0) is usually derived from direct solar observations. However to mitigate instrument calibration errors other methods have been developed using solar monthly means [40] or radiance means over reference sectors where low concentrations of the target molecule are expected [62,94]. Li et al. [159] employed instead the principal components of the radiances in regions with low concentrations of SO_2 to capture the radiance variability caused by physical processes and measurement artifacts. By fitting these principal components and SO_2 Jacobians calculated with a RTM, they retrieve directly SO_2 VCDs.

The second step involves the calculation of AMFs. For optically thin absorbers, AMFs can be calculated by decoupling the radiative transfer calculation of vertically resolved sensitivities (W(z)) and a-priori vertical profile shapes (S(z)) [206] as shown in Eq. (5).

$$AMF = \int_0^\infty W(z)S(z)dz \qquad (5)$$

The W(z), known as scattering weight, represents the number of times the radiation reaching the satellite has traversed an atmospheric layer (z, z+dz) (middle left panels of Fig. 2) while the S(z), known as shape factor, is the normalized trace gas profile (middle right panels of Fig. 2).

Fig. 2 shows that between 300 nm and 500 nm the photon penetration varies slowly with wavelength, particularly for altitudes above 2 km. It is therefore a fair approximation to compute AMFs using a single wavelength representative of the vertical sensitivities across the fitting window. Below 2 km the photon penetration at those wavelengths is greatly reduced limiting the sensitivity of satellite measurements to the boundary layer. Retrievals of SO_2, H_2CO, and BrO carried out in the UV spectral range (between ∼ 320 nm and 360 nm) are particularly affected by the reduction of sensitivity to the boundary layer.

Usually the scattering weights, computed with a RTM, are parameterized by observational angles, terrain/cloud pressure, and terrain/cloud reflectivity at the instrument's field-of-view (FOV)

and stored in a LUT. The effect of clouds is modeled by using the cloud radiance fraction and the cloud pressure. Due to sparseness of observations and large spatial and temporal variabilities, information of a-priori profiles is obtained from CTMs. Differences in the spatial and temporal resolution between the CTM and the satellite observations, the ability of CTMs to simulate the vertical distribution of the absorbing species, the geometry-dependent surface reflectance properties and the presence of aerosols and clouds are the most significant sources of error in AMF calculations [169]. It is worth mentioning that despite being a significant source of error, aerosols are not considered explicitly in most retrievals given the difficulty to disentangle the effect of scattering by clouds and aerosols. The lower panel of Fig. 2 shows vertically resolved AMFs of NO_2, SO_2, H_2CO, BrO, $C_2H_2O_2$ and H_2O computed using photon paths and shape factors shown in Fig. 2 middle panels.

3.4. Algorithm physics

The challenges met in algorithm physics development allow fitting to very close to the noise levels of the atmospheric spectra, often to several times 10^{-4} of the measured radiance [cf., 222]. Reaching this level of fitting precision requires reference data, including absorption spectra, which cumulatively contribute less than this amount to the fitting uncertainties.

Solar reference spectrum. An accurate solar reference spectrum is required to support in-orbit wavelength calibration [43], Ring effect determination [50], determination of the instrument transfer function from flight data [43] and correction for spectral undersampling [43,45]. There are low-resolution extraterrestrial solar spectra that are very accurate in absolute intensity calibration [250]. These have been combined with a ground-based FTS spectrum from [146] at the National Solar Observatory, supplemented at wavelengths < 305 nm by balloon-based spectra from [103] to produce a high-resolution spectrum with accurate intensity calibration [46].

Rayleigh scattering and the Ring effect. Rayleigh scattering is often the predominant contributor to back scattered light measured in the nadir, particularly for wavelengths shorter than 500 nm. Highly accurate parameterizations of the wavelength dependences of the cross sections and scattering phase functions for Rayleigh scattering by air are available [9,19,50], with [19] being the current preference.

Grainger and Ring [100] first noticed that solar Fraunhofer lines became broadened and reduced in depth depending on the SZA when viewed from the ground in scattered sunlight. This is now known to be the effect of inelastic scattering by the fraction of the Rayleigh scattering by air that is inelastic, i.e., Raman scattering. The Raman scattering, about 97% rotational Raman and the rest vibrational Raman, constitutes 4% of the Rayleigh scattering in the wavelengths considered here. Ring effect corrections are performed using the molecular physics of the Raman scattering [50] coupled with the solar reference spectrum [46], and in some cases coupled with radiative transfer calculations [127,267] to the level that negligible uncertainties remain in the spectral fitting from this source of spectral structure [cf. 43].

Vibrational Raman scattering in ocean water can be readily measured in these wavelengths (it must be corrected for in the spectral analysis for some gases) and it is suggested that it may be used to estimate chlorophyll and dissolved organic matter contents of ocean water [259].

Wavelength issues. Shifts from ground-based wavelength calibration can be seen on orbit due to launch stresses or the different thermal environment. It can also vary by substantial amounts, compared to the spectral fitting needs, due to thermal and other in-flight perturbations and instrumental effects (e.g., orbital or seasonal thermal changes, partial filling of the field-of-view). Additionally, solar irradiances are obtained at substantially different Doppler shifts (up to 0.01 nm at 400 nm) from Earth-view radiance measurements.

For these reasons, Caspar and Chance [38] showed that wavelength calibration is improved by using a Fraunhofer reference spectrum, [revised in 46], and applying either spectral cross-correlation [145] or nonlinear least-squares (NLLS) fitting to adjust window portions of radiances or irradiances. These methods can usually calibrate in vacuum wavelength to 0.01 detector pixel spacing or better [cf. 43]. The NLLS method has been implemented in operational algorithms for GOME, SCIAMACHY, OMI and OMPS.

Instrument function and sampling issues. Slit functions (instrument transfer functions, ITFs) may differ in flight from those determined in ground calibration. It is often useful to re-determine them in flight, combining this with the wavelength calibration using NLLS.

Nyquist sampling of a spectrum requires sampling to at least twice the highest spatial (i.e., wavelength) frequency admitted by the resolution limit of the instrument [the band limit, 93]. Spectral undersampling occurs when spectral measurements are not made at fine enough spacing to Nyquist sample the ITF [45] and thus provide full knowledge of the spectrum up to the band limit. Undersampling can be a major source of fitting error in the current generation of satellite-borne spectrometers, particularly as they mostly do not take enough spectral samples relative to their spectral resolution and, as the solar irradiance spectra must be resampled in wavelength in order to be compared to radiances in the spectral fitting process, aliasing occurs [43]. Where the trace gas absorptions are optically thin, it is possible to correct for most of the undersampling error. It is also now possible to quantitatively determine the amount a spectrum will be undersampled (or, how close it is to being fully-sampled) for a given instrument configuration during the design phase [45].

Reference spectra. Reference spectra for UV and VIS measurements are now included in the HITRAN database [97] and regularly updated. Reference spectra are published sometimes with vacuum wavelengths and sometimes with air wavelengths. It is highly recommended that vacuum wavelengths be the standard, and that accurate conversion be made when necessary. Highly accurate conversion formulae are available [19]. As UV and VIS reference spectra are increasingly determined using Fourier transform spectrometers, this becomes less of an issue, since they measure frequencies, usually in wavenumbers (cm^{-1}), and these are intrinsically in vacuum. Table 3 gives the current recommendations for UV and VIS reference spectra. Files containing the current recommended spectra and treatments for the Ring effect and spectral undersampling are available from kchance@cfa.harvard.edu.

4. Trace gas retrievals and applications

4.1. Ozone

Singer and Wentworth [237] proposed a method to determine the vertical distribution of O_3 using satellite observations. Following their seminal work, the first measurements of O_3 using satellite observations date back to the 1960s. Venkateswaran et al. [261] used the Chappuis bands around 600 nm unlike most studies which benefited from measurements made by instruments designed to study backscattered solar radiation in the UV [4,123,134,216].

In April 8, 1970, the Nimbus 4 satellite was launched as part of the Nimbus program to collect weather and meteorological data. One of its payloads, the Backscatter UltraViolet (BUV) instrument was the first satellite instrument specifically designed to carry on O_3 observations [141]. Since then the concentrations of O_3 have been monitored continuously from space. The Total Ozone Moni-

Table 3
Recommended reference spectra and Raman treatments.

Molecule or effect	Range [nm] (vacuum)	Temperature(s) [K]	Resolution FWHM
O_3 [a]	195–660	218, 228, 243, 273, 295	0.02 nm
NO_2 [b]	238–667, 280–337	220, 294	1.1658 cm−1
SO_2 [c]	227–417	203, 223, 243, 273, 293	0.21-0.26 nm
H_2CO [d]	300–386	223, 233, 243, 253, 263, 273, 283, 293	0.8721 cm^{-1}
$C_2H_2O_2$ [e]	370–470	296	0.01 nm
H_2O [f]	440–450	Atmospheric average [f]	0.003 nm [f]
BrO [g]	286–383	228	10.49 cm−1
IO [h]	409–474	298	0.07 nm
OClO [i]	312–441	213, 233, 253, 273, 293	1.0 cm-1
Oxygen collision complex (O_2-O_2) [j]	336–601	203, 293	0.32-0.45 nm [j]
Raman (Ring effect) [k]	200–1001	selectable	selectable
H_2O (l) Raman [l]	200–1001		
Undersampling [m]	N/A	N/A	Instrument-dependent
Solar reference spectrum [n]	200–1001	Solar T	0.04 nm

[a] Derived from [26,27,56,98,173] and [232] are an alternate choice.
[b] [258]
[c] [22]
[d] [47]
[e] Derived from [265]
[f] [104]. [97] is an alternate source. HITRAN improvements incorporating [104] are underway.
[g] [281]
[h] [180]
[i] Derived from [135]
[j] [245]
[k] [50]
[l] Derived from [271]
[m] [45]
[n] [46]

toring Spectrometer (TOMS) [107] is a NASA instrument designed to detect the total amount of atmospheric O_3 on a daily global scale. Launched aboard Nimbus-7 (November 1978–May 1993), Meteor-3 (August 1991–November 1994), ADEOS (July 1996–June 1997), and Earth Probe (July 1996 December 2005) TOMS played a pivotal role in monitoring the evolution of the O_3 hole [92,112]. Another O_3 monitoring payload of Nimbus 7 was the Solar Backscatter UltraViolet (SBUV) designed to monitor the vertical distribution of stratospheric O_3 with a vertical resolution of ~ 7 km above the O_3 layer. This monitoring activity was followed by the SBUV/2 family on-board NOAA weather satellites (1984 to now) [87]. The merged total O_3 (MOD) and profile data sets were developed using the SBUV version 8.6 processor [184]. This algorithm implements inter-instrument calibration of the radiance guaranteeing the consistency of the record [14]. The accuracy of the data sets is proven to be within 5% with respect to high-resolution in-situ and satellite measurements [133,147]. The original MOD time series is being expanded with data from OMPS-NP on S-NPP and NOAA-20 satellites.

Chehade et al. [51] used the synergy between multiple satellite sensors including BUV, SBUV and SBUV/2, to analyze the long-term trend of total O_3 over 1979–2012. They found noticeable correlations between the equivalent stratospheric chlorine and the downward trend in O_3 over 1979–1997. The evolution of the Ozone Hole is monitored by TOMS, SBUV, SBUV/2, OMI, GOME-1, GOME-2, OMPS-NM and OMPS-NP with recovery detected recently as a result of adherence to the Montreal Protocol [238,279].

To provide information about tropospheric O_3 crucial to unravel its complex origin, several tropospheric O_3 residual methods were developed by subtracting the stratospheric O_3 amount from the total O_3 column [e.g., 85,301,302]. Direct estimates of O_3 profiles with sensitivity to the lower troposphere like the ones shown in Fig. 3 are possible thanks to hyperspectral sensors such as GOME-1, OMI, GOME-2, and OMPS-NM [5,33,105,117,136,165,166,191,194,196,255,256].

Sauvage et al. [226] compared the simulations performed using the GEOS-Chem CTM with GOME-1 observations in the tropics.

In addition to providing top-down constraint on biomass burning emissions, they improved the spatial distribution of lightning NO_x emissions, which in turn, mitigated the discrepancy between the model and the satellite. Similarly, Zhang et al. [294] studied the potential causes of disagreement between the O_3 columns simulated by the global model and observed from TES and OMI sensors. They attributed the low biased tendency of the model over the tropics to the underestimation of emissions from a combination of sources including those from lightning, biomass burning, and biogenic soil. On the other hand, the model was high biased at higher latitudes due to uncertainties associated with the stratospheric-tropospheric exchange.

Satellites have paved the way for studying the spatio-temporal variations of tropospheric O_3 at a high spatial resolution where other types of observations are rather scarce[167]. provided an observational evidence from GOME that tropospheric ozone in the Tibetan Plateau in June can be exceptionally low mainly due to the Asian summer monsoon. Despite the limitations associated with the low sensitivity of the UV satellites to tropospheric O_3 Kar et al. [129] demonstrated that they have the potential for detecting urban O_3 plumes occurring episodically. To improve the sensitivity of nadir UV satellite measurements to O_3 in the free troposphere, multi-instrument retrievals have been developed combining the UV Hartley–Huggins and thermal infrared O_3 bands [55,90,91].

4.2. Nitrogen dioxide

Nitrogen dioxide (NO_2), produced during combustion, is designated as a criteria pollutant by the US Environmental Protection Agency (EPA) owing to its negative effects on public health and the environment. It is regulated as nitrogen oxides (NO_x = NO_2 +NO), which are precursors of O_3 and particulate matter, both of which are also criteria pollutants that have important implications for human health, crop yields, and climate. Monitoring of NO_2 concentrations is essential because NO_2 is a toxic gas at high concentrations. Epidemiological studies indicate that exposure to moderate levels
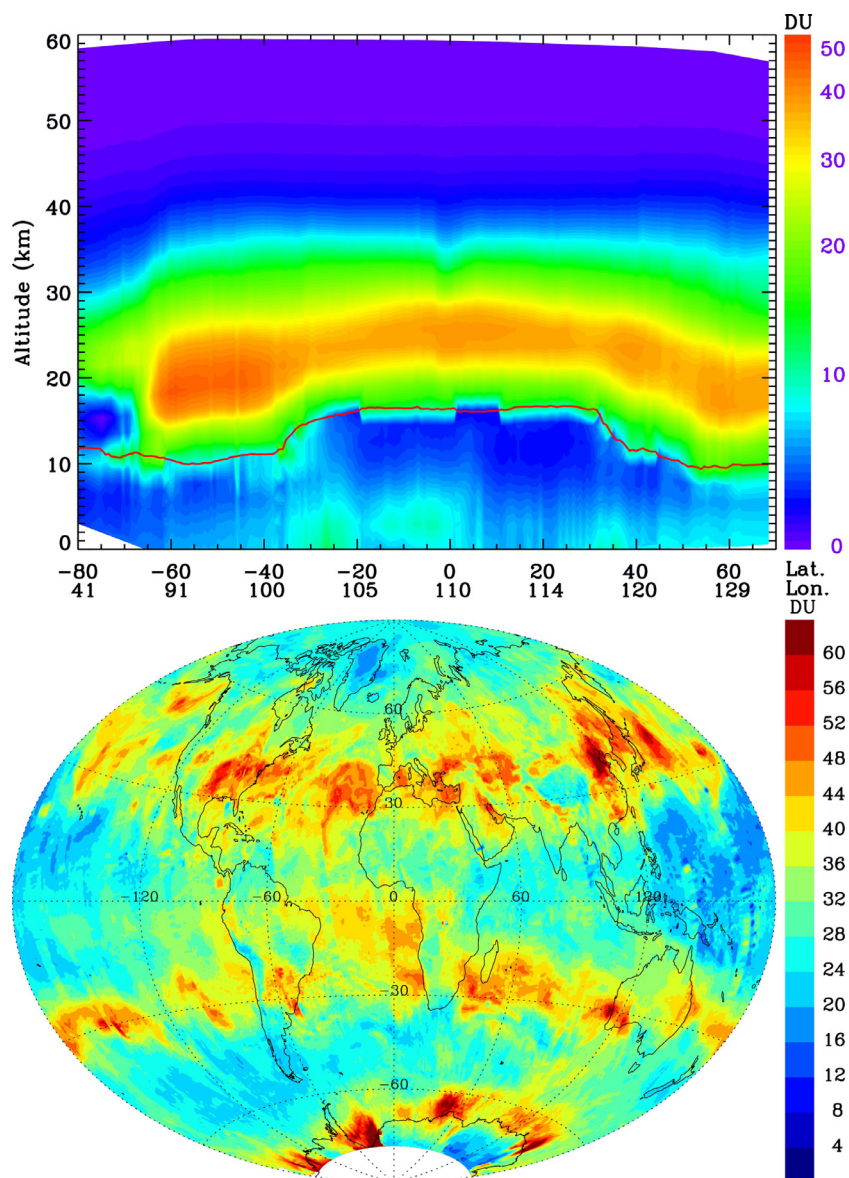
Fig. 3. Upper panel shows an orbit of partial (layer) column O_3 (DU) profiles retrieved using GOME-1 measurements for orbit 71022024 on 22 October 1997. The red lines indicates the tropopause height. Lower pannel shows a global map of OMI tropospheric O_3 column on 26 August 2006 gridded to $0.5°$ longitude $\times$ $0.5°$ latitude grid cells. Some systematic cross-track position dependent biases have been removed before gridding by assuming these data do not vary with cross-track position within a month.

of NO_2 increases bronchitis and reduces lung function in children and asthmatics [29,75].

NO_2 observations from satellite remote sensing provide consistent, long-term global data that complement existing ground-based networks. Satellite NO_2 data have been widely used to detect and quantify NO_x emission-related anthropogenic activities of large point sources such as coal-fired power plants in the US [58,71], China [275,295], and India [170], and of large area sources such as cities in the US [57,148,171] and around the world [69,139]. For instance, Fig. 4 shows dramatic declines in tropospheric NO_2 over the US, western Europe, and Japan as observed by OMI from 2005 to 2017 while the opposite trends are found in some other parts of the world. Moreover, satellite NO_2 observations have been frequently used to evaluate CTMs [e.g., 121,131,214,215], and study NO_x chemistry, lifetime and deposition [e.g., 149,204,251].

NO_2 observations from satellite remote sensing exploit strong NO_2 absorption features in the VIS and near UV. Spectroscopic ground-based measurements of NO_2 date back nearly four decades [e.g., 25]. They have evolved to a new generation of instruments to measure total (e.g., Pandora, [111]) and tropospheric NO_2 columns (e.g., Multi Axis DOAS, MAXDOAS). The first global tropospheric NO_2 observations were made in the middle 1990s with GOME-1 [31]. Similar measurements, but at higher spatial resolution, were continued with SCIAMACHY [23], OMI [158], GOME-2 [195] and more recently TROPOMI [260].

Determination of the abundance of atmospheric NO_2 from satellite instruments is performed by direct fit and DOAS algorithms in the 330 nm to 500 nm spectral range [20,21,28,175,179,217,254,285]. The spectral fit procedure yields the NO_2 SCD, which represents the integrated abundance of NO_2 along the average photon path through the atmosphere. Subsequent retrieval step of the NO_2 product includes the calculation of AMF to convert the SCD into a VCD. Since the satellite-retrieved SCDs contain both tropospheric and stratospheric contributions, a separation algorithm is necessary to estimate stratospheric and tropospheric NO_2 VCDs. To properly separate the two components, the current approach is to use near-local observations over unpolluted and cloudy areas [e.g., 11,28]. This approach takes
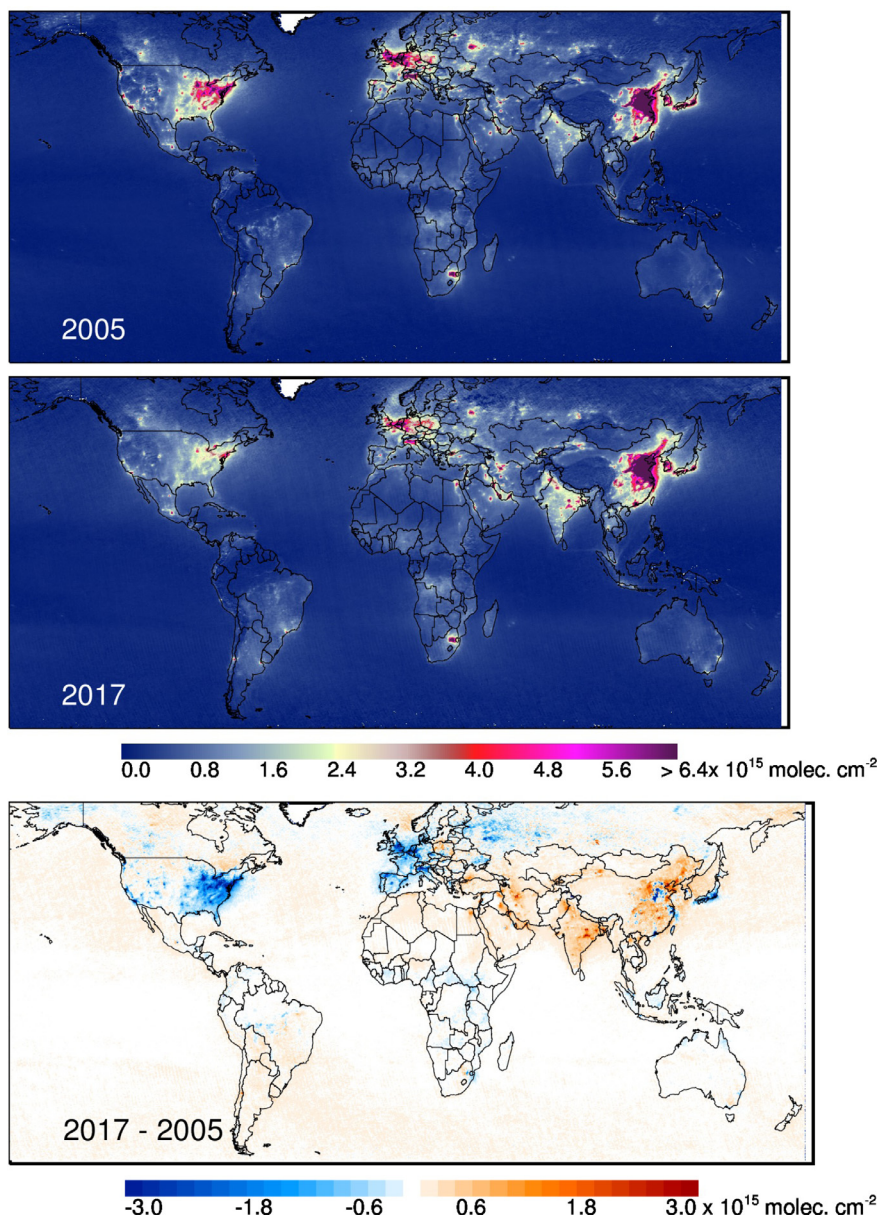
Fig. 4. Annual average OMI tropospheric NO_2 VCDs at 0.25° latitude × 0.25° longitude spatial resolution for 2005 (top) and 2017 (middle). Bottom panel shows changes in tropospheric NO_2 VCDs between 2005 and 2017.

advantage of the large contribution of stratospheric NO_2 (90%) to the total NO_2 column in unpolluted (e.g., non-coastal oceans) and overcast areas [179] and derives stratospheric NO_2 field by spatial interpolation and smoothing of NO_2 observations over those areas. An alternative to separate the trospospheric and stratospheric components is data assimilation [e.g., 20].

Estimating measurement uncertainties in satellite-observed NO_2 is critical for allowing informed use of the data, interpretation and assimilation of the data using models and estimation of errors in satellite-derived higher level products (e.g., surface NO_2 concentration, NO_x emissions). Current error estimates for satellite NO_2 products are based on the error propagation from the measurement noise with SCDs errors (typically 0.8×10^{15} molecules cm^{-2}) resulting from spectral fitting itself [175,291] and AMF errors (30-80%) arising from various input parameters used in AMF calculations [28].

4.3. Sulfur dioxide

SO_2 in the atmosphere can impact climate and air quality on local to global scales. SO_2 is primarily produced from anthropogenic sources through the burning of fossil fuels, with smaller contributions from the smelting of sulfur-containing ores. Natural sources of SO_2 include the oxidation of dimethyl sulfide from marine phytoplankton and volcanic activity, with small contributions from biomass burning and soil and vegetation decay. In the atmosphere, SO_2 forms sulfate aerosols, which can have regional to global effects on climate [197]. When SO_2 is injected into the stratosphere during a strong volcanic eruption, the resulting sulfate aerosols may persist for over a year [181], significantly influencing the Earth's radiation budget. Volcanic aerosols and SO_2 can also pose a danger to aircraft. The wet and dry deposition that removes sulfur from the atmosphere results in acid deposition to

the Earths surface. SO_2 and its resulting sulfate increase mortality and morbidity rates with significant consequences for public health [213,283].

The strong SO_2 absorption band in the ultraviolet was first exploited to make SO_2 measurements from space using the TOMS [140] and SBUV [185] instruments on the Nimbus-7 satellite during the 1982 El Chichón volcanic eruptions. Later, observations from TOMS and SBUV/2 were used to track the global transport of SO_2 from the 1991 Pinatubo eruption [16,102,183], and TOMS instruments have been used to produce over two decades of volcanic observations [35,142].

With the advent of GOME-1 hyperspectral UV measurements, it became possible to measure lower levels of SO_2 pollution from anthropogenic emissions and small volcanic eruptions [74]. SO_2 has been measured by SCIAMACHY [2,154], GOME-2 [18,203,220], OMI [137,161,247,288] and OMPS [161,286,296]. These measurements have been used to study trends over time [82,83,139,162,163,172,276], sulfur deposition [79,204], emissions and inventories [80,81,132,153,164,182] and volcanic fluxes [34,37,246], as well as in aviation safety applications [24,36,138].

SO_2 retrievals in the UV are complicated by the presence of O_3 absorption and strong molecular Rayleigh scattering. SO_2 retrievals have typically used the wavelength range of 310–330 nm, where light is not fully extinguished by the O_3 bands or Rayleigh scattering, and where SO_2 absorption contains strong differential spectral features. However, strong O_3 absorption in this spectral region means uncertainties in O_3 column amount and instrument calibration can drastically affect SO_2 retrievals, and both O_3 and Rayleigh scattering cause the AMF to change significantly as a function of SO_2 height and wavelength. Uncertainties are particularly prominent for volcanic cases, where plume height may be uncertain, significant aerosol loading can occur, and in the case of large SO_2 loading, there is non-linearity in the backscatter radiance due to the suppression of photon scattering inside the plume.

The different altitude penetration depths at different wavelengths due to O_3 and Rayleigh scattering can, however, provide information on SO_2 plume height, and have been exploited to retrieve plume height in cases of moderate and large volcanic eruptions [203,289,290]. Several retrieval approaches have been applied to improve SO_2 retrievals in the UV, including weighting function DOAS [154], iterative spectral fitting [288,289], optimal estimation [203], principal component analysis (PCA) [159,161], and the use of the weaker SO_2 absorption feature in the 360–390 nm region for strong volcanic cases [18,248]. Despite these approaches, SO_2 retrievals often suffer from high biases in the background (greater than 100%), particularly at high SZA, which often necessitate empirical bias corrections either by retrieval algorithms [e.g., 248] or in post-processing science studies [e.g., 83].

Declining SO_2 emissions in developed countries [132,139] mean that anthropogenic SO_2 is becoming more difficult to measure from space using most current spaceborne instruments. However, the deployment of instruments with increasingly high spatial resolution in LEO and GEO orbits will allow the resolution of individual plumes and facilitate high-accuracy emission estimation. Applications of new retrieval techniques may also provide new opportunities in the applications of UV SO_2 data. For example, near-real-time retrievals of volcanic plume height enabled by machine learning [e.g., 73] have potential uses in aviation safety management, the monitoring of geoengineering using SO_2 to produce sulfate aerosol [e.g., 199] and the study of volcanic effects on climate.

4.4. Formaldehyde

Global observations of H_2CO from space were first reported using GOME-1 measurements. Chance et al. [48] used a direct fit of the distinct H_2CO absorption in the UV to derive SCDs and

RTM calculations of AMFs to convert them to VCDs [206]. After this seminal work, retrievals of H_2CO have been developed with SCIAMACHY, OMI, GOME2-A/B, S-NPP OMPS-NM and TROPOMI measurements [59,62,63,94,96,114,144,160,268,282,291]. Oxidation of CH_4 and NMVOCs are the major sources of atmospheric H_2CO. Background levels are determined by CH_4 oxidation. Secondary production due to oxidation of VOCs from vegetation, biomass burning, on-road vehicles and industry [6,299] or direct emissions from industry is the origin of regional enhancements.

The H_2CO lifetime of few hours favours its utilization as a satellite-derived proxy for VOCs emissions. Considerable amounts of research exploiting this application have provided top-down constraints on bottom-up biomass burning and biogenic VOC emissions inventories used in chemical transport models [10,174,192,193,242,243]. Shim et al. [233] performed a Bayesian inversion of global isoprene emissions using GOME-1 H_2CO columns from September 1996 to August 1997. Their inversion estimate mitigated the underestimation of isoprene emissions (50%), particularly over the tropics. Changing the global biogenic emissions reduced OH concentration by 11% in the model, showing that satellite derived H_2CO provides information on the oxidation capacity of the atmosphere [125,253]. Likewise, Palmer et al. [205] provided an optimal estimation of isoprene emissions over North America using GOME-1 observations. They found a 25% seasonal bias associated with biogenic emissions higher (lower) at the beginning (end) of the growing season.

The long-term stability of the OMI sensor and inter calibration efforts has allowed the observation of multi-decadal trends of H_2CO around the world [7,53,54,60,61,126,239,300]. De Smedt et al. [61] studied long-term trends of H_2CO using GOME-1 and SCIAMACHY observations between 1997 and 2009. Enhanced anthropogenic VOC emissions caused by rapid economic and population growth in China and India, resulted in positive H_2CO trends. Opposite to this behaviour, cities in Japan and the Northeast U.S. underwent downward trends reflecting the effectiveness of emission control policies. OMI revealed positive trends over China [60,239] with the exception of the Pearl River Delta, a region where air quality has improved due to controls on VOC emissions imposed by the eleventh five-year-plan [297]. Zhu et al. [300] reported trends of OMI H_2CO columns across North America in the 2005–2014 period. Reduction of H_2CO was observed in the Houston-Galveston-Brazoria area, home to petrochemical facilities [53,300] while columns increased in the Cold Lake Oil sands in Canada in line with the rapid increase in crude oil production.

Despite all these scientific applications of current and past H_2CO retrievals, challenges owing to small H_2CO atmospheric optical depth still need to be addressed. For individual pixels the random error of the SCD dominates the uncertainty with values between 100% and 300% [60] depending on the instrument SNR. These random errors can be reduced by averaging in the spatial and temporal domain at the cost of reduced resolutions. Systematic uncertainties in the slant column determination are linked to the choice of reference cross sections and fitting parameters. A-priori information used in AMF calculations (surface reflectance properties, vertical distribution of H_2CO, cloud contamination, presence of aerosols) is also affected by uncertainties [169]. It is of paramount importance for the development of robust products suitable for use in chemical forecast and data assimilation to use consistent reference data and a-priori information. For example, while González Abad et al. [96] use [47] De Smedt et al. use [190] H_2CO cross sections. To reduce SCD fitting uncertainties and reduce interference from other trace gases active in the same spectral range such as BrO higher spectral resolution instruments will help. However, designs based on dispersing grating spectrometers make SNR and spectral resolution compete against each other.
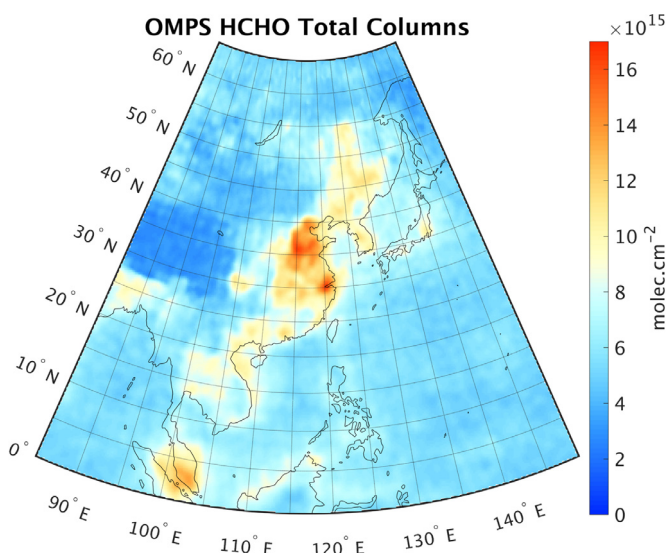
Fig. 5. H_2CO columns observed by the OMPS-NM sensor on-board S-NPP satellite over East Asia. Observations for the months of June and July 2015 are over-sampled to a 27×27 km^2 grid. H_2CO enhancements linked to urban concentrations can be appreciated over China, South Korea and Japan as well as biogenic and pyrogenic signatures in Indonesia.

Initiatives like the QA4ECV [291] program and the NASA's MEaSUREs program aim to develop robust, reliable and traceable data records extending multiple decades combining measurements by multiple instruments deployed in different space crafts. These initiatives require fiducial correlative datasets to perform validation studies. Until recent years H_2CO validation records were sparse. Recent advances in ground-based remote sensing [124,240,262] and in-situ aircraft measurements [39,88,219] result in rigorous validation exercises [263,298]. Developing a strategy to perform these studies in a consistent way across instruments and locations is a-priority to increase the value of H_2CO satellite datasets. Fig. 5 shows East Asia S-NPP OMPS-NM H_2CO retrievals during KORUS-AQ [240] where there are correlative ground-based and aircraft measurements. These field experiments provide opportunities to validate not only satellite data but also a-priori information used in the retrievals.

4.5. Bromine monoxide

Odd bromine chemistry is a significant contributor to global O_3 loss, particularly due to synergistic chemical cycles with odd chlorine chemistry [224,266]. Its main stratospheric sources are CH_3Br (partly natural, partly anthropogenic), halons (currently being largely phased out) and, increasingly, very short-lived substances containing bromine [208]. Tropospheric sources include polar spring rapid release [e.g., 1,15,106,236], volcanos [e.g., 17], salt lakes [e.g., 109] and stratospheric transport [223]. Polar Spring BrO enhancements are known to be associated with boundary layer O_3 depletion [52]. Measurements of BrO have been used together with chemical and dynamical modeling to investigate stratospheric versus tropospheric enhancements of atmospheric BrO at high northern latitudes, including the effects of very short lived stratospheric bromocarbons, such as CH_2Br_2, in the total BrO columns [223,252].

BrO was initially expected to be measurable from space in regions with stratospheric enhancements. While this enhancements are associated with the polar vortices, sensitivity studies for SCIAMACHY and GOME-1 determined that BrO should be measurable globally [49]. When spectra from GOME-1 became available there were four nearly simultaneous publications of initial BrO measurements [43,110,212,218]. Each demonstrated the expected variation of stratospheric BrO with SZA and each saw localized enhancements, apparently in the troposphere, at high latitudes. Hegels et al. [110], Platt and Wagner [212], Richter et al. [218] used the DOAS approach for spectral analysis [211] while Chance [43] directly fitted the radiance spectra. Chance [43] also introduced the use of in-flight wavelength calibration using a solar reference spectrum [38,46,50], the undersampling correction [cf. 45], the rotational Raman (Ring) correction including the O_2 ground state $^3\Sigma^-g$ structure [50], and the now widely used common-mode correction. BrO is measured in the $A^2\Pi_{3/2} \leftarrow X^2\Pi_{3/2}$ ultraviolet transition, in spectral windows centered near 350 nm. Additional molecular absorbers included in the fitting are normally O_3, NO_2, $OClO$, H_2CO, SO_2, and the O_2–O_2 collision complex.

After the initial GOME-1 studies demonstrated that BrO is one of the easier trace molecules to measure from space in these wavelengths, satellite BrO retrievals were developed using SCIAMACHY [e.g., 257], GOME-2 [e.g., 249], OMI [e.g., 118,144,244], OMPS-NM [95], and TROPOMI [231] radiances. Hörmann et al. [118] monitored the seasonal cycle of BrO formation over the Rann of Kutch, one of the largest salt marshes in the world, using OMI and GOME-2 observations. They concluded that the Rann of Kutch is one of the strongest natural sources of BrO outside the polar regions possibly having significant impacts in the local and regional O_3 chemistry. Enhancements of BrO over the Great Salt Lake and the Dead Sea have also been observed by OMI [118,244]. High concentration of BrO was observed in the plume of the Ambrym volcano eruption in 2005 by [44] confirming previous ground-based observations [17]. Later studies have identified BrO in at least several different volcano plumes [119] including the Kasatochi 2008 eruption [249] and the Eyjafjallajökull 2010 [113,220].

4.6. Water vapor

Water vapor is one of the state variables measured since the beginning of the satellite era. Here, we only focus on the satellite measurements made in the visible wavelength range. Total Column Water Vapor (TCWV, also referred to as Integrated Water Vapor or Precipitable Water Vapor) can be retrieved in the near red, red, and blue wavelength range using the spectra obtained by GOME-1 [150,201,270], SCIAMACHY [202,210], GOME-2 [101] and OMI [272]. The GOME-1, SCIAMACHY and GOME-2 TCWV derived from the red spectral range [101] are combined into a homogenized monthly climate product at $1°$ horizontal resolution from July 1995 to December 2015 [12].

TCWV retrievals in the near red and red spectral range use the DOAS method or its variations. As water vapor absorption is relatively strong in this spectral region, individual lines can get saturated when TCWV is large. Since individual spectral lines are not resolved by the instruments, the measured differential absorption varies non-linearly with the actual TCWV. This non-linear saturation effect needs to be corrected in the retrieval.

TCWV can also be derived from the blue spectral range [269], as shown by the example in Fig. 6 [272,273]. Given the weak absorption of water vapor in the blue wavelength range, it is not necessary to perform any saturation correction for the SCDs, though the fitting uncertainty is larger compared to that for the red spectral range due to reduced SNR, especially when TCWV is low (< 10 mm). Since GOME-1, SCHIAMACHY and GOME-2 all cover the blue wavelength range, they can be combined with OMI to generate a long-term TCWV dataset.

Water vapor is crucial for understanding Earth's climate. It is the predominant greenhouse gas in the atmosphere and can amplify the warming associated with other greenhouse gases, such as CO_2 and CH_4. Water vapor is also important for the hydrological cycle and energy budget. Through condensation, it leads to cloud
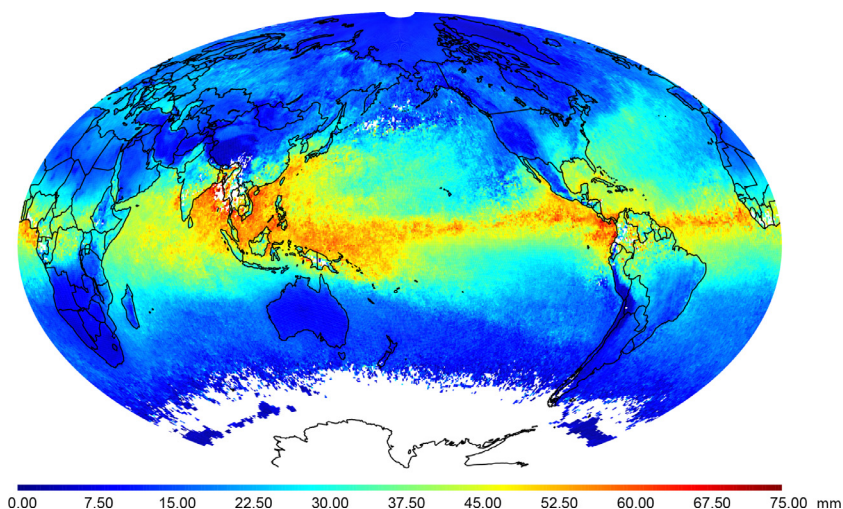
Fig. 6. Global TCWV observed by the OMI instrument. Only observations with cloud fractions below 5% for the months of June, July and August 2006 are included in the average at each $0.5° \times 0.5°$ grid.

formation and latent heat release, directly influencing the weather and atmospheric circulation. The tropospheric profile, stratospheric profile and total column of H_2O vapor are included by the Global Climate Observing System as ECVs that critically contribute to the characterization of the climate system (https://www.ncdc.noaa.gov/gosic/gcos-essential-climate-variable-ecv-data-access-matrix). TCWV can be calculated by integrating water vapor profiles or retrieved from visible/NIR/IR/Microwave/GPS observations.

Water vapor is highly variable in space and time. Thus, observations on a variety of spatio-temporal scales are required to characterize its distribution. Many in-situ and remote sensing techniques are used to measure water vapor concentration or total column from ground stations, aircrafts and satellites. Ground-based data provide nice temporal coverage; Aircraft data provide fine vertical resolution; Satellite data provide global perspective.

A review of satellite derived water vapor data is provided by the GEWEX Water Vapor Assessment [228]. These data result from satellite remote sensing in the visible/NIR/Shortwave IR/IR/microwave/GPS wavelength range. Each dataset has its own resolution, spatial and temporal coverage and characteristics. For example, data from GPS occultation are available for all weather conditions, but have relatively sparse spatial coverage; data from microwave observations are available for both clear-sky and cloudy-sky conditions, but are affected by precipitation and are usually available only over the oceans; data from NIR and shortwave IR observations are typically available only over land and are strongly affected by clouds; data from IR observations are available over both land and the oceans, but have low sensitivity in the boundary layer and are strongly affected by clouds; data from visible observations are sensitive to the boundary layer and are available for all surface types, but are strongly affected by clouds.

Satellite TVWC products are typically validated against measurements from ground-based networks, such as the radiosondes of the GCOS Reference Upper-Air Network (GRUAN) [230], the GPS data of the International GNSS Service archived at NCAR [274] or SuomiNet GPS data provided by UCAR [278], and the microwave radiometer data of the Department of Energy ARM program [32]. These reference datasets are usually accurate and precise to sub-mm level [65,200] and are well suited for satellite data validation. The version 2 sun photometer data from AERONET [116] has a dry bias of 5% and an estimated uncertainty of 13% [209]. Version 3 AERONET data released in 2018 are expected to have better quality and may be useful for satellite data validation.

Since most of the ground-based stations are over land, validation over the ocean is usually conducted against the TCWV derived from satellite microwave sensors. Microwave observations of TCWV are considered to have high quality over the ice-free non-precipitating ocean [188,189]. Remote Sensing Systems provides Version 7 TCWV data for SSM/I, SSMIS, AMSRE, and WindSat on $0.25° \times 0.25°$ grid over the oceans twice per day. These data have also been homogenized into a monthly $1° \times 1°$ climate data record starting in 1988 [187]. Alternatively, the EUMETSAT Satellite Application Facility on Climate Monitoring provides $0.5° \times 0.5°$ 6-hourly and monthly TCWV climate data records (1987–2014) derived from SSM/I and SSMIS using the Hamburg Ocean Atmosphere Parameters and Fluxes from Satellite Data Version 4 algorithm (https://wui.cmsaf.eu/safira/action/viewProduktSearch).

In addition satellite datasets that compare well with the reference data mentioned above may be useful for validation. In particular, the TCWV retrieved from the OCO-2 shortwave IR data [198] and the TCWV integrated using the COSMIC GPS radio occultation profiles [115] may serve as references.

4.7. Glyoxal

The possibility of observing $C_2H_2O_2$ from space was first suggested by Volkamer et al. [264], after they observed high concentrations in Mexico City. Their observations translated to satellite optical depths of up to 1.7×10^{-3} in the 400 nm–500 nm spectral range, however typical optical depths of $C_2H_2O_2$ are usually much smaller ($\sim 10^{-4}$). Given the current capabilities of VIS space-borne detectors and the typical amount of $C_2H_2O_2$ these are the most challenging retrievals discussed here. Adding to the problem is the limited amount of measurements for validation. Ground-based remote sensing measurements of $C_2H_2O_2$ are also affected by high uncertainties derived from its weak absorption and in-situ measurements of $C_2H_2O_2$ in field campaigns are scarce. Despite these adversities several $C_2H_2O_2$ retrievals have been developed over the years.

The first global observations of $C_2H_2O_2$ were derived using GOME-1 and SCIAMACHY measurements [44,282]. Subsequent efforts have resulted in the development of GOME-2 [156,268] and OMI $C_2H_2O_2$ retrievals [3,40]. The work by Wittrock et al. [282] showed spatial correlations between $C_2H_2O_2$ and H_2CO. This is because both species are short-lived products of VOC oxidation, with isoprene being the dominant precursor of both.

Studying the ratio of $C_2H_2O_2$ and H_2CO can provide insights into the VOC precursors and chemical pathways leading to their formation [41,42,128,268,282]. Vrekoussis et al. [268] found a noticeable decreasing trend between the $C_2H_2O_2$ to H_2CO ratio and NO_2 columns over major cities around the world using GOME-2 data, which they suggest could be driven by shifts in the identity of predominant anthropogenic VOC precursors. Using the GEOS-Chem model and OMI data Chan Miller et al. [42] tested the $C_2H_2O_2$ yield from isoprene and its dependence on nitrogren oxides. They found that the formation of $C_2H_2O_2$ is dominated by the isomerization of isoprene peroxy radicals under low nitrogen oxide conditions. Kaiser et al. [128] used a combined set of OMI and aircraft observations over the Southeast US to evaluate the effectiveness of using this ratio as a hydrocarbon source indicator. They found that regions with high $C_2H_2O_2$ to H_2CO ratio were primarily associated with monoterpene emissions, whereas isoprene-rich areas led to comparatively lower values.

Stavrakou et al. [241] carried on inverse modeling experiments using SCIAMACHY data over continents. These studies reveled significant $C_2H_2O_2$ chemical transport models underestimations. Space-based constraints on direct VOC emissions from biogenic, pyrogenic and anthropogenic emissions partially reduced the underestimation of the simulated $C_2H_2O_2$ columns but it resulted in large overestimations of surface $C_2H_2O_2$ concentrations. Adding a secondary formation pathway of an unspecified precursor they found it to be the largest contributor (50%) to the $C_2H_2O_2$ budget. This ambiguity underscores the importance of improving our understanding of $C_2H_2O_2$ formation if realistic top-down constraints on the relevant emissions are to be provided [41,234].

5. Conclusion

The 1970 launch of the BUV instrument as a payload on-board Nimbus-4 initiated the era of global and regular space observations of atmospheric O_3. Since then, the evolution and improvement of space instruments able to observed the Earth's atmosphere has been remarkable. The BUV instrument was capable of measuring twelve spectral channels with a spatial resolution of 200×200 km^2, achieving global coverage in ten days. TROPOMI, launched in 2017, has hyperspectral capabilities covering the 270–775 nm range with a spatial resolution of 3.5×7 km^2 and daily global coverage. Future GEO instruments (GEMS, TEMPO and Sentinel 4) will also measure at high spatial resolution while providing hourly observations. Early instruments enabled the development of O_3 and SO_2 retrievals. Later instruments, thanks to their hyperspectral capabilities, allowed retrievals of other trace gases including tropospheric O_3, NO_2, H_2CO, H_2O, BrO and $C_2H_2O_2$.

The information provided by these retrievals is valuable to understand a broad range of scientific questions with important societal implications. After the early studies monitoring the evolution of stratospheric O_3, the improvement of space-based instrument capabilities has led to investigations on atmospheric chemistry and atmospheric dynamics, studies assessing the impact of air quality policies and economic activity in pollution trends and transport and epidemiologic studies quantifying the health implications of pollution on a global scale.

Looking to the future, the value of historic records and future measurements can be further expanded by developing long-term, consistent data records using inter-calibrated measurements from different instruments. These long-term records will help monitor the current and past global change of the Earth system, reducing the uncertainty in the trends derived from them and providing a solid baseline to calibrate future missions.

As scientific retrievals become mature and ready to transition into operational frameworks, improving the characterization of errors is imperative. Data assimilation and air quality managers need

detailed retrieval error information to fully exploit them. Recent efforts to increase the amount and quality of reference measurements for satellite validation should be exploited to establish rigorous validation procedures.

Ensuring the continuity of current LEO measurements and GEO missions should be a priority. The planned follow up missions to GEMS (East Asia) and Sentinel-4 (Europe) instruments extend into the third decade of the first century. Over North America, the TEMPO mission has a required operational period of two years (contractually extendable up to ten years) with no follow up mission currently planned. In the future it will be desirable to extend the spatial coverage of GEO observations to South America, Africa and Oceania.

The continuous push towards higher spatial resolution results in enormous amounts of data. New retrieval frameworks together with optimized processing and distribution data centers are necessary to ensure near-real time production of higher level products dependent on this satellite retrievals such as chemical forecasts. After fifty years of development and evolution, space-based instruments and retrievals designed to monitor O_3 and air quality are ready to become part of our social push for healthier life styles.

Acknowledgments

References

[1] Abbatt JPD, Thomas JL, Abrahamsson K, Boxe C, Granfors A, Jones AE, et al. Halogen activation via interactions with environmental ice and snow in the polar lower troposphere and other regions. Atmos Chem Phys 2012;12(14):6237–71. doi:10.5194/acp-12-6237-2012. https://www.atmos-chem-phys.net/12/6237/2012/.

[2] Afe OT, Richter A, Sierk B, Wittrock F, Burrows JP. Bro emission from volcanoes: a survey using gome and sciamachy measurements. Geophys Res Lett 2004;31(24):L24113. doi:10.1029/2004GL020994. https://www.agupubs.onlinelibrary.wiley.com/doi/abs/10.1029/2004GL020994.

[3] Alvarado LMA, Richter A, Vrekoussis M, Wittrock F, Hilboll A, Schreier SF, et al. An improved glyoxal retrieval from OMI measurements. Atmos Meas Tech 2014;7(12):4133–50. doi:10.5194/amt-7-4133-2014. https://www.atmos-meas-tech.net/7/4133/2014/.

[4] Anderson G, Barth C, Cayla F, London J. Satellite observations of the vertical ozone distribution in the upper stratosphere (ozone vertical distribution in upper stratosphere determined from OGO 4 observations, describing calibration of satellite data and onboard instrumentation). Ann Geophys 1969;25:341–5.

[5] Bak J, Liu X, Kim J-H, Haffner DP, Chance K, Yang K, et al. Characterization and correction of OMPS nadir mapper measurements for ozone profile retrievals. Atmos Meas Tech 2017;10(11):4373–88. doi:10.5194/amt-10-4373-2017. https://www.atmos-meas-tech.net/10/4373/2017/.

[6] Barkley MP, De Smedt I, Van Roozendael M, Kurosu TP, Chance K, Arneth A, et al. Top-down isoprene emissions over tropical south america inferred from SCIAMACHY and OMI formaldehyde columns. J Geophys Res Atmos 2013;118(12):6849–68. doi:10.1002/jgrd.50552. https://www.agupubs.onlinelibrary.wiley.com/doi/full/10.1002/jgrd.50552.

[7] Barkley MP, González Abad G, Kurosu TP, Spurr R, Torbatian S, Lerot C. OMI air-quality monitoring over the middle east. Atmos Chem Phys 2017;17(7):4687–709. doi:10.5194/acp-17-4687-2017. https://www.atmos-chem-phys.net/17/4687/2017/.

[8] Barrie L. An integrated global atmospheric chemistry observations strategy and WMOs leading role: GAW & IGACO. In: Seminar on global Earth-system monitoring, 5–9 September 2005. Shinfield Park, Reading: ECMWF; 2006. p. 35–41. https://www.ecmwf.int/node/7954.

[9] Bates D. Rayleigh scattering by air. Planet Space Sci 1984;32(6):785–90. doi:10.1016/0032-0633(84)90102-8. http://www.sciencedirect.com/science/article/pii/0032063384901028.

[10] Bauwens M, Stavrakou T, Müller J-F, De Smedt I, Van Roozendael M, van der Werf GR, et al. Nine years of global hydrocarbon emissions based on source inversion of OMI formaldehyde observations. Atmos Chem Phys 2016;16(15):10133–58. doi:10.5194/acp-16-10133-2016. https://www.atmos-chem-phys.net/16/10133/2016/acp-16-10133-2016.html.

[11] Beirle S, Hörmann C, Jöckel P, Liu S, Penning de Vries M, Pozzer A, et al. The STRatospheric estimation algorithm from mainz (STREAM): estimating strato-

spheric NO_2 from nadir-viewing satellites by weighted convolution. Atmos Meas Tech 2016;9(7):2753–79. doi:10.5194/amt-9-2753-2016. https://www.atmos-meas-tech.net/9/2753/2016/.

[12] Beirle S, Lampel J, Wang Y, Mies K, Dörner S, Grossi M, et al. The ESA GOME-evolution "climate" water vapor product: a homogenized time series of h_2o columns from GOME, SCIAMACHY, and GOME-2. Earth Syst Sci Data 2018;10(1):449–68. doi:10.5194/essd-10-449-2018. https://www.earth-syst-sci-data.net/10/449/2018/.

[13] Bernath PF, McElroy CT, Abrams MC, Boone CD, Butler M, Camy-Peyret C, et al. Atmospheric chemistry experiment (ACE): mission overview. Geophys Res Lett 2005;32(15). doi:10.1029/2005GL022386. https://www.agupubs.onlinelibrary.wiley.com/doi/abs/10.1029/2005GL022386.

[14] Bhartia PK, McPeters RD, Flynn LE, Taylor S, Kramarova NA, Frith S, et al. Solar backscatter UV (SBUV) total ozone and profile algorithm. Atmos Meas Tech 2013;6(10):2533–48. doi:10.5194/amt-6-2533-2013. https://www.atmos-meas-tech.net/6/2533/2013/.

[15] Blechschmidt A-M, Richter A, Burrows JP, Kaleschke L, Strong K, Theys N, et al. An exemplary case of a bromine explosion event linked to cyclone development in the arctic. Atmos Chem Phys 2016;16(3):1773–88. doi:10.5194/acp-16-1773-2016. https://www.atmos-chem-phys.net/16/1773/2016/.

[16] Bluth GJ, Doiron SD, Schnetzler CC, Krueger AJ, Walter LS. Global tracking of the SO_2 clouds from the june, 1991 mount pinatubo eruptions. Geophys Res Lett 1992;19(2):151–4. doi:10.1029/91GL02792. https://www.agupubs.onlinelibrary.wiley.com/doi/abs/10.1029/91GL02792.

[17] Bobrowski N, Hönninger G, Galle B, Platt U. Detection of bromine monoxide in a volcanic plume. Nature 2003;423:273–6. doi:10.1038/nature01625. https://doi.org/10.1038/nature01625.

[18] Bobrowski N, Kern C, Platt U, Hörmann C, Wagner T. Novel SO_2 spectral evaluation scheme using the 360–390 nm wavelength range. Atmos Meas Tech 2010;3(4):879–91. doi:10.5194/amt-3-879-2010. http://www.atmos-meas-tech.net/3/879/2010/.

[19] Bodhaine BA, Wood NB, Dutton EG, Slusser JR. On rayleigh optical depth calculations. J Atmos Ocean Technol 1999;16(11):1854–61. doi:10.1175/1520-0426(1999)016<1854:ORODC>2.0.CO;2. https://doi.org/10.1175/1520-0426(1999)016(1854:ORODC)2.0.CO;2.

[20] Boersma KF, Eskes HJ, Dirksen RJ, van der A RJ, Veefkind JP, et al. An improved tropospheric NO_2 column retrieval algorithm for the ozone monitoring instrument. Atmos Meas Tech 2011;4:1905–28. doi:10.5194/amt-4-1905-2011. https://www.atmos-meas-tech.net/4/1905/2011/.

[21] Boersma KF, Eskes HJ, Richter A, De Smedt I, Lorente A, Beirle S, et al. Improving algorithms and uncertainty estimates for satellite NO_2 retrievals: results from the quality assurance for essential climate variables (QA4ecv) project. Atmos Meas Tech 2018;11:6651–78. doi:10.5194/amt-11-6651-2018. https://www.atmos-meas-tech.net/11/6651/2018/.

[22] Bogumil K, Orphal J, Homann T, Voigt S, Spietz P, Fleischmann O, et al. Measurements of molecular absorption spectra with the SCIAMACHY preflight model: instrument characterization and reference data for atmospheric remote-sensing in the 230–2380 nm region. J Photochem Photobiol A 2003;157(2):167–84. doi:10.1016/S1010-6030(03)00062-5. http://www.sciencedirect.com/science/article/pii/S1010603003000625.

[23] Bovensmann H, Burrows JP, Buchwitz M, Frerick J, Noël S, Rozanov VV, et al. SCIAMACHY: Mission objectives and measurement modes. J Atmos Sci 1999;56(2):127–50. doi:10.1175/1520-0469(1999)056<0127:SMOAMM>2.0.CO;2. https://journals.ametsoc.org/doi/10.1175/1520-0469(1999)056(0127:SMOAMM)2.0.CO;2.

[24] Brenot H, Theys N, Clarisse L, van Geffen J, van Gent J, Van Roozendael M, et al. Support to aviation control service (SACS): an online service for near-real-time satellite monitoring of volcanic plumes. Hazards Earth Syst Sci 2014;14:1099–123. doi:10.5194/nhess-14-1099-2014. https://www.nat-hazards-earth-syst-sci.net/14/1099/2014/.

[25] Brewer AC, McElroy CT, Kerr JB. Nitrogen dioxide concentrations in the atmosphere. Nature 1973;246:129–33. doi:10.1038/246129a0. https://doi.org/10.1038/246129a0.

[26] Brion J, Chakir A, Charbonnier J, Daumont D, Parisse C, Malicet J. Absorption spectra measurements for the ozone molecule in the 350–830 nm region. J Atmos Chem 1998;30(2):291–9. doi:10.1023/A:1006036924364. https://doi.org/10.1023/A:1006036924364.

[27] Brion J, Chakir A, Daumont D, Malicet J, Parisse C. High-resolution laboratory absorption cross section of o_3. temperature effect. Chem Phys Lett 1993;213(5):610–12. doi:10.1016/0009-2614(93)89169-I. http://www.sciencedirect.com/science/article/pii/000926149389169I.

[28] Bucsela EJ, Krotkov NA, Celarier EA, Lamsal LN, Swartz WH, Bhartia PK, et al. A new stratospheric and tropospheric NO_2 retrieval algorithm for nadir-viewing satellite instruments: application to OMI. Atmos Meas Tech 2013;6:2607–26. doi:10.5194/amt-6-2607-2013. https://www.atmos-meas-tech.net/6/2607/2013/.

[29] Burnett RT, Stieb D, Brook JR, Cakmak S, Dales R, Raizenne M, et al. Associations between short-term changes in nitrogen dioxide and mortality in canadian cities. AEH 2004;59(5):228–36. doi:10.3200/AEOH.59.5.228-236. https://doi.org/10.3200/AEOH.59.5.228-236.

[30] . The remote sensing of tropospheric composition from space. Burrows JP, Platt U, Borrell P, editors. Berlin Heidelberg: Springer-Verlag; 2011. ISBN 978-3-642-14790-6. doi:10.1007/978-3-642-14791-3. https://www.springer.com/us/book/9783642147906.

[31] Burrows JP, Weber M, Buchwitz M, Rozanov V, Ladstätter-Weißenmayer A, Richter A, et al. The global ozone monitoring experiment (GOME): mission concept and first scientific results. J Atmos Sci 1999;56(2):151–75. doi:10.1175/1520-0469(1999)056<0151:TGOMEG>2.0.CO;2.

[32] Cadeddu MP, Liljegren JC, Turner DD. The atmospheric radiation measurement (ARM) program network of microwave radiometers: instrumentation, data, and retrievals. Atmos Meas Tech 2013;6(9):2359–72. doi:10.5194/amt-6-2359-2013. https://www.atmos-meas-tech.net/6/2359/2013/amt-6-2359-2013.html.

[33] Cai Z, Liu Y, Liu X, Chance K, Nowlan CR, Lang R, et al. Characterization and correction of global ozone monitoring experiment 2 ultraviolet measurements and application to ozone profile retrievals. J Geophys Res Atmos 2012;117(D7). doi:10.1029/2011JD017096. https://agupubs.onlinelibrary.wiley.com/doi/abs/10.1029/2011JD017096.

[34] Carn S, Clarisse L, Prata A. Multi-decadal satellite measurements of global volcanic degassing. J Volcanol Geotherm Res 2016;311:99–134. doi:10.1016/j.jvolgeores.2016.01.002. https://www.sciencedirect.com/science/article/pii/S0377027316000032?via%3Dihub.

[35] Carn SA, Krueger AJ, Bluth GJS, Schaefer SJ, Krotkov NA, Watson IM, et al. Volcanic eruption detection by the total ozone mapping spectrometer (TOMS) instruments: a 22-year record of sulphur dioxide and ash emissions. Geol Soc Lond Sp Publ 2003;213(1):177–202. doi:10.1144/GSL.SP.2003.213.01.11. http://sp.lyellcollection.org/lookup/doi/10.1144/GSL.SP.2003.213.01.11.

[36] Carn SA, Krueger AJ, Krotkov NA, Yang K, Evans K. Tracking volcanic sulfur dioxide clouds for aviation hazard mitigation. Nature Haz 2009;51(2):325–43. doi:10.1007/s11069-008-9228-4. https://link.springer.com/article/10.1007%2Fs11069-008-9228-4.

[37] Carn SA, Yang K, Prata AJ, Krotkov NA. Extending the long-term record of volcanic SO_2 emissions with the ozone mapping and profiler suite nadir mapper. Geophys Res Lett 2015;42(3):925–32. doi:10.1002/2014GL062437. https://agupubs.onlinelibrary.wiley.com/doi/abs/10.1002/2014GL062437.

[38] Caspar C, Chance K. GOME wavelength calibration using solar and atmospheric spectra. In: Third ERS symposium on Space at the service of our environment, 414; 1997. p. 609. http://adsabs.harvard.edu/abs/1997ESASP.414.609C.

[39] Cazorla M, Wolfe GM, Bailey SA, Swanson AK, Arkinson HL, Hanisco TF. A new airborne laser-induced fluorescence instrument for in situ detection of formaldehyde throughout the troposphere and lower stratosphere. Atmos Meas Tech 2015;8:541–52. doi:10.5194/amt-8-541-2015. https://www.atmos-meas-tech.net/8/541/2015/.

[40] Chan Miller C, González Abad G, Wang H, Liu X, Kurosu T, Jacob DJ, et al. Glyoxal retrieval from the ozone monitoring instrument. Atmos Meas Tech 2014;7(11):3891–907. doi:10.5194/amt-7-3891-2014. https://www.atmos-meas-tech.net/7/3891/2014/.

[41] Chan Miller C, Jacob DJ, González Abad G, Chance K. Hotspot of glyoxal over the pearl river delta seen from the OMI satellite instrument: implications for emissions of aromatic hydrocarbons. Atmos Chem Phys 2016;16(7):4631–9. doi:10.5194/acp-16-4631-2016. https://www.atmos-chem-phys.net/16/4631/2016/.

[42] Chan Miller C, Jacob DJ, Marais EA, Yu K, Travis KR, Kim PS, et al. Glyoxal yield from isoprene oxidation and relation to formaldehyde: chemical mechanism, constraints from SENEX aircraft observations, and interpretation of OMI satellite data. Atmos Chem Phys 2017;17(14):8725–38. doi:10.5194/acp-17-8725-2017. https://www.atmos-chem-phys.net/17/8725/2017/.

[43] Chance K. Analysis of BrO measurements from the global ozone monitoring experiment. Geophys Res Lett 1998;25(17):3335–8. doi:10.1029/98GL52359. https://agupubs.onlinelibrary.wiley.com/doi/abs/10.1029/98GL52359.

[44] Chance K. Spectroscopic measurements of tropospheric composition from satellite measurements in the ultraviolet and visible: steps toward continuous pollution monitoring from space. In: Perrin A, Ben Sari-Zizi N, Demaison J, editors. Remote sensing of the atmosphere for environmental security. NATO security through science series NATO security through science series C: environmental security. NATO security through science series. Dordrecht: Springer; 2006. p. 1–25. doi:10.1007/978-1-4020-5090-9_1.

[45] Chance K, Kurosu TP, Sioris CE. Undersampling correction for array detector-based satellite spectrometers. Appl Opt 2005;44(7):1296–304. doi:10.1364/AO.44.001296. https://www.osapublishing.org/ao/abstract.cfm?uri=ao-44-7-1296.

[46] Chance K, Kurucz RL. An improved high-resolution solar reference spectrum for Earth's atmosphere measurements in the ultraviolet, visible, and near infrared. J Quant Spectrosc Radiat Transf 2010;111(9):1289–95. doi:10.1016/j.jqsrt.2010.01.036. http://www.sciencedirect.com/science/article/pii/S0022407310000610.

[47] Chance K, Orphal J. Revised ultraviolet absorption cross sections of H_2CO for the HITRAN database. J Quant Spectrosc Radiat Transf 2011;112:1509–10. doi:10.1016/j.jqsrt.2011.02.002. http://www.sciencedirect.com/science/article/pii/S002240731100080X.

[48] Chance K, Palmer PI, Spurr RJD, Martin RV, Kurosu TP, Jacob DJ. Satellite observations of formaldehyde over North America from GOME. Geophys Res Lett 2000;27(21):3461–4. doi:10.1029/2000GL011857. https://agupubs.onlinelibrary.wiley.com/doi/abs/10.1029/2000GL011857.

[49] Chance KV, Burrows JP, Schneider W. Retrieval and molecule sensitivity studies for the global ozone monitoring experiment and the scanning imaging absorption spectrometer for atmospheric chartography. In: Remote sensing of atmospheric chemistry, 1491. SPIE; 1991. p. 151–66. doi:10.1117/12.46657. https://doi.org/10.1117/12.46657.

[50] Chance KV, Spurr RJD. Ring effect studies: rayleigh scattering, including molecular parameters for rotational raman scattering, and the fraunhofer

spectrum. Appl Opt 1997;36(21):5224–30. doi:10.1364/AO.36.005224. https://www.osapublishing.org/ao/abstract.cfm?uri=ao-36-21-5224.

[51] Chehade W, Weber M, Burrows JP. Total ozone trends and variability during 1979–2012 from merged data sets of various satellites. Atmos Chem Phys 2014;14(13):7059–74. doi:10.5194/acp-14-7059-2014. https://www.atmos-chem-phys.net/14/7059/2014/.

[52] Choi S, Theys N, Salawitch RJ, Wales PA, Joiner J, Canty TP, et al. Link between arctic tropospheric BrO explosion observed from space and sea-salt aerosols from blowing snow investigated using ozone monitoring instrument BrO data and GEOS-5 data assimilation system. J Geophys Res Atmos 2018;123(13):6954–83. doi:10.1029/2017JD026889. https://agupubs.onlinelibrary.wiley.com/doi/abs/10.1029/2017JD026889.

[53] Choi Y, Souri AH. Chemical condition and surface ozone in large cities of texas during the last decade: observational evidence from OMI, CAMS, and model analysis. Rem Sens Environ 2015;168:90–101. doi:10.1016/j.rse.2015.06.026. http://www.sciencedirect.com/science/article/pii/S0034425715300559.

[54] Choi Y, Souri AH. Seasonal behavior and long-term trends of tropospheric ozone, its precursors and chemical conditions over iran: a view from space. Atmos Environ 2015;106:232–40. doi:10.1016/j.atmosenv.2015.02.012. http://www.sciencedirect.com/science/article/pii/S1352231015001314.

[55] Cuesta J, Eremenko M, Liu X, Dufour G, Cai Z, Höpfner M, et al. Satellite observation of lowermost tropospheric ozone by multispectral synergism of IASI thermal infrared and GOME-2 ultraviolet measurements over europe. Atmos Chem Phys 2013;13(19):9675–93. doi:10.5194/acp-13-9675-2013. https://www.atmos-chem-phys.net/13/9675/2013/.

[56] Daumont D, Brion J, Charbonnier J, Malicet J. Ozone UV spectroscopy i: absorption cross-sections at room temperature. JAtmos Chem 1992;15(2):145–55. doi:10.1007/BF00053756. https://doi.org/10.1007/BF00053756.

[57] de Foy B, Lu Z, Streets DG. Impacts of the control strategies, the great recession and weekday variations on NO2 columns above North American cities. Atmos Environ 2016;138:74–86. doi:10.1016/j.atmosenv.2016.04.038. http://www.sciencedirect.com/science/article/pii/S1352231016303211.

[58] de Foy B, Lu Z, Streets DG, Lamsal LN, Duncan BN. Estimates of power plant NO$_x$ emissions and lifetimes from OMI NO2 satellite retrievals. Atmos Environ 2015;116:1–11. doi:10.1016/j.atmosenv.2015.05.056. http://www.sciencedirect.com/science/article/pii/S1352231015301291.

[59] De Smedt I, Müller J-F, Stavrakou T, van der A R, Eskes H, Van Roozendael M. Twelve years of global observations of formaldehyde in the troposphere using GOME and SCIAMACHY sensors. Atmos Chem Phys 2008;8:4947–63. doi:10.5194/acp-8-4947-2008. https://www.atmos-chem-phys.net/8/4947/2008/.

[60] De Smedt I, Stavrakou T, Hendrick F, Danckaert T, Vlemmix T, Pinardi G, et al. Diurnal, seasonal and long-term variations of global formaldehyde columns inferred from combined OMI and GOME-2 observations. Atmos Chem Phys 2015;15(21):12519–45. doi:10.5194/acp-15-12519-2015. https://www.atmos-chem-phys.net/15/12519/2015/.

[61] De Smedt I, Stavrakou T, Müller J-F, van der A RJ, Van Roozendael M. Trend detection in satellite observations of formaldehyde tropospheric columns. Geophys Res Lett 2010;37(18). doi:10.1029/2010GL044245. https://www.agupubs.onlinelibrary.wiley.com/doi/abs/10.1029/2010GL044245.

[62] De Smedt I, Theys N, Yu H, Danckaert T, Lerot C, Compernolle S, et al. Algorithm theoretical baseline for formaldehyde retrievals from s5p TROPOMI and from the QA4ECV project. Atmos Meas Tech 2018;11(4):2395–426. doi:10.5194/amt-11-2395-2018. https://www.atmos-meas-tech.net/11/2395/2018/.

[63] De Smedt I, Van Roozendael M, Stavrakou T, Müller J-F, Lerot C, Theys N, et al. Improved retrieval of global tropospheric formaldehyde columns from GOME-2/metop-a addressing noise reduction and instrumental degradation issues. Atmos Meas Tech 2012;5(11):2933–49. doi:10.5194/amt-5-2933-2012. https://www.atmos-meas-tech.net/5/2933/2012/.

[64] DeLand MT, Cebula RP. NOAA 11 Solar backscatter ultraviolet, model 2 (SBUV/2) instrument solar spectral irradiance measurements in 1989–1994: 2. results, validation, and comparisons. J Geophys Res Atmos 1998;103(D13):16251–73. doi:10.1029/98JD01204. https://agupubs.onlinelibrary.wiley.com/doi/abs/10.1029/98JD01204.

[65] Dirksen RJ, Sommer M, Immler FJ, Hurst DF, Kivi R, Vömel H. Reference quality upper-air measurements: GRUAN data processing for the vaisala RS92 radiosonde. Atmos Meas Tech 2014;7(12):4463–90. doi:10.5194/amt-7-4463-2014. https://www.atmos-meas-tech.net/7/4463/2014/.

[66] Dobrolenskiy Y, Dziuban I, Ivanov Y, Syniavskyi I, Ionov D, Poberovsky A, et al. Optical design of imaging spectrometer for atmosphere monitoring from near-Earth orbit. In: Optical design and engineering VII, 10690. SPIE; 2018. p. 10690–8. doi:10.1117/12.2312021.

[67] Dobrolenskiy YS, Ionov DV, Korablev OI, Fedorova AA, Zherebtsov EA, Shatalov AE, et al. Development of a space-borne spectrometer to monitor atmospheric ozone. Appl Opt 2015;54(11). doi:10.1364/AO.54.003315. https://www.osapublishing.org/ao/abstract.cfm?uri=ao-54-11-3315.

[68] Dobson GMB. A photoelectric spectrophotometer for measuring the amount of atmospheric ozone. Proc Phys Soc 1931;43(3):324–39. doi:10.1088/0959-5309/43/3/308.

[69] Duncan BN, Lamsal LN, Thompson AM, Yoshida Y, Lu Z, Streets DG, et al. A space-based, high-resolution view of notable changes in urban NO$_x$ pollution around the world (2005–2014). J Geophys Res 2016;121:976–96. doi:10.1002/2015JD024121. https://agupubs.onlinelibrary.wiley.com/doi/abs/10.1002/2015JD024121.

[70] Duncan BN, Prados AI, Lamsal LN, Liu Y, Streets DG, Gupta P, et al. Satellite data of atmospheric pollution for u.s. air quality applications: examples of applications, summary of data end-user resources, answers to FAQs, and common mistakes to avoid. Atmos Environ 2014;94:647–62. doi:10.1016/j.atmosenv.2014.05.061. http://www.sciencedirect.com/science/article/pii/S1352231014004270.

[71] Duncan BN, Yoshida Y, de Foy B, Lamsal LN, Streets D, Lu Z, et al. The observed response of the ozone monitoring instrument (OMI) NO2 column to NO$_x$ emission controls on power plants in the united states: 2005–2011. Atmos Environ 2013;81:102–11. doi:10.1016/j.atmosenv.2013.08.068. http://www.sciencedirect.com/science/article/pii/S1352231013006894.

[72] Earth Observation Portal. Satellite missions directory - earth observation missions - eoportal. https://directory.eoportal.org/web/eoportal/satellite-missions.

[73] Efremenko DS, Loyola R DG, Hedelt P, Spurr RJD. Volcanic SO2 plume height retrieval from UV sensors using a full-physics inverse learning machine algorithm. Int J Remote Sen 2017;38(sup1):1–27. doi:10.1080/01431161.2017.1348644. https://www.tandfonline.com/doi/full/10.1080/01431161.2017.1348644.

[74] Eisinger M, Burrows JP. Tropospheric sulfur dioxide observed by the ERS-2 GOME instrument. Geophys Res Lett 1998;25(22):4177–80. doi:10.1029/1998GL900128. http://doi.wiley.com/10.1029/1998GL900128.

[75] EPA. Integrated science assessment for oxides of nitrogen – health criteria (First External Review Draft). Tech. Rep.. U.S. Environmental Protection Agency, Research Triangle Park,NC 27711; 2008. EPA/600/R-07/093

[76] ESA. Global ozone monitoring experiment GOME users manual. 1995. https://earth.esa.int/documents/10174/1596664/GOME05.pdf.

[77] Fabry C, Buisson H. L'absorption de l'ultra-violet par l'ozone et la limite du spectre solaire. J Phys Theor Appl 1913;3(1):196–206. doi:10.1051/jphystap:019130030019601. https://hal.archives-ouvertes.fr/jpa-00241833.

[78] Fabry C, Buisson H. Étude de l'extrémité ultra-violette du spectre solaire. J Phys Radium 1921;2(7):197–226. doi:10.1051/jphysrad:0192100207019700. https://hal.archives-ouvertes.fr/jpa-00204283.

[79] Fedkin NM, Li C, Dickerson RR, Canty T, Krotkov NA. Linking improvements in sulfur dioxide emissions to decreasing sulfate wet deposition by combining satellite and surface observations with trajectory analysis. Atmos Environ 2019;199:210–23. doi:10.1016/J.ATMOSENV.2018.11.039. https://www.sciencedirect.com/science/article/pii/S1352231018308197.

[80] Fioletov VE, McLinden CA, Krotkov N, Li C. Lifetimes and emissions of SO2 from point sources estimated from OMI. Geophys Res Lett 2015;42(6):1969–76. doi:10.1002/2015GL063148. http://doi.wiley.com/10.1002/2015GL063148.

[81] Fioletov VE, McLinden CA, Krotkov N, Li C, Joiner J, Theys N, et al. A global catalogue of large SO2 emissions derived from the ozone monitoring instrument. Atmos Chem Phys 2016;16(18):11497–519. doi:10.5194/acp-16-11497-2016. https://www.atmos-chem-phys.net/16/11497/2016/.

[82] Fioletov VE, McLinden CA, Krotkov N, Moran MD, Yang K. Estimation of SO2 emissions using OMI retrievals. Geophys Res Lett 2011;38(21):L21811. doi:10.1029/2011GL049402. http://doi.wiley.com/10.1029/2011GL049402.

[83] Fioletov VE, McLinden Ca, Krotkov N, Yang K, Loyola DG, Valks P, et al. Application of OMI, SCIAMACHY, and GOME-2 satellite SO2 retrievals for detection of large emission sources. J Geophys Res Atmos 2013;118(19):11,399–11,418. doi:10.1002/jgrd.50826. http://doi.wiley.com/10.1002/jgrd.50826.

[84] Fishman J, Bowman KW, Burrows JP, Richter A, Chance KV, Edwards DP, et al. Remote sensing of tropospheric pollution from space. Bull Am Meteorol Soc 2008;89(6):805–22. doi:10.1175/2008BAMS2526.1. https://journals.ametsoc.org/doi/10.1175/2008BAMS2526.1.

[85] Fishman J, Watson CE, Larsen JC, Logan JA. Distribution of tropospheric ozone determined from satellite data. J Geophys Res Atmos 1990;95(D4):3599–617. doi:10.1029/JD095iD04p03599. https://agupubs.onlinelibrary.wiley.com/doi/abs/10.1029/JD095iD04p03599.

[86] Fleig AJ, McPeters RD, Taylor L. Nimbus 7 solar backscatteru ltraviolet (SBUV) spectral scans solar irradiance and earth radiance product user's guide. NASA Reference Publication 1234; 1990. p. 130. https://ntrs.nasa.gov/archive/nasa/casi.ntrs.nasa.gov/19900007911.pdf.

[87] Frederick SE, Cebula RP, Heath DF. Instrument characterization for the detection of long-term changes in stratospheric ozone: an analysis of the SBUY/2 radiometer. J Atmos Ocean Technol 1986;3(3):472–80. doi:10.1175/1520-0426(1986)003<0472:ICFTDO>2.0.CO;2.

[88] Fried A, Crawford J, Olson J, Walega J, Potter W, Wert B, et al. Airborne tunable diode laser measurements of formaldehyde during TRACE-p: distributions and box model comparisons. J Geophys Res Atmos 2003;108(D20). doi:10.1029/2003JD003451. https://agupubs.onlinelibrary.wiley.com/doi/abs/10.1029/2003JD003451.

[89] Frith SM, Kramarova NA, Stolarski RS, McPeters RD, Bhartia PK, Labow GJ. Recent changes in total column ozone based on the SBUV version 8.6 merged ozone data set. J Geophys Res Atmos 2014;119(16):9735–51. doi:10.1002/2014JD021889. https://agupubs.onlinelibrary.wiley.com/doi/abs/10.1002/2014JD021889.

[90] Fu D, Kulawik SS, Miyazaki K, Bowman KW, Worden JR, Eldering A, et al. Retrievals of tropospheric ozone profiles from the synergism of AIRS and OMI: methodology and validation. Atmos Meas Tech 2018;11(10):5587–605. doi:10.5194/amt-11-5587-2018. https://www.atmos-meas-tech.net/11/5587/2018/.

[91] Fu D, Worden JR, Liu X, Kulawik SS, Bowman KW, Natraj V. Characterization of ozone profiles derived from aura TES and OMI radiances. Atmos Chem Phys 2013;13(6):3445–62. doi:10.5194/acp-13-3445-2013. https://www.atmos-chem-phys.net/13/3445/2013/.

[92] Gleason JF, Bhartia PK, Herman JR, McPeters R, Newman P, Stolarski RS, et al. Record low global ozone in 1992. Science 1993;260(5107):523–6. doi:10.1126/science.260.5107.523. http://science.sciencemag.org/content/260/5107/523.

[93] Goldman S. Information theory. Prentice-Hall,; 1953.

[94] González Abad G, Liu X, Chance K, Wang H, Kurosu TP, Suleiman R. Updated smithsonian astrophysical observatory ozone monitoring instrument (SAO OMI) formaldehyde retrieval. Atmos Meas Tech 2015;8:19–32. doi:10.5194/amt-8-19-2015. https://www.atmos-meas-tech.net/8/19/2015/.

[95] González Abad G, Liu X, Suleiman RM, Saiz-Lopez A, Chance K. SAO OMPS bromine monoxide retrievals. AGU fall meeting abstracts; 2017.

[96] González Abad G, Vasilkov A, Seftor C, Liu X, Chance K. Smithsonian astrophysical observatory ozone mapping and profiler suite (SAO OMPS) formaldehyde retrieval. Atmos Meas Tech 2016;9(7):2797–812. doi:10.5194/amt-9-2797-2016. https://www.atmos-meas-tech.net/9/2797/2016/.

[97] Gordon IE, Rothman LS, Hill C, Kochanov RV, Tan Y, Bernath PF, et al. The HITRAN2016 molecular spectroscopic database. J Quant Spectrosc Radiat Transf 2017;203:3–69. doi:10.1016/j.jqsrt.2017.06.038. http://www.sciencedirect.com/science/article/pii/S0022407317301073.

[98] Gorshelev V, Serdyuchenko A, Weber M, Chehade W, Burrows JP. High spectral resolution ozone absorption cross-sections – part 1: measurements, data analysis and comparison with previous measurements around 293 k. Atmos Meas Tech 2014;7(2):609–24. doi:10.5194/amt-7-609-2014. https://www.atmos-meas-tech.net/7/609/2014/.

[99] Götz FWP, Meetham AR, Dobson GMB. The vertical distribution of ozone in the atmosphere. Proc R Soc A Contain Pap Math Phys Char 1934;145(855):416–46.

[100] Grainger JF, Ring J. Anomalous fraunhofer line profiles. Nature 1962;193:762. doi:10.1038/193762a0.

[101] Grossi M, Valks P, Loyola D, Aberle B, Slijkhuis S, Wagner T, et al. Total column water vapour measurements from GOME-2 metop-a and metop-b. Atmos Meas Tech 2015;8(3):1111–33. doi:10.5194/amt-8-1111-2015. https://www.atmos-meas-tech.net/8/1111/2015/.

[102] Guo S, Bluth GJS, Rose WI, Watson IM, Prata AJ. Re-evaluation of SO2 release of the 15 june 1991 pinatubo eruption using ultraviolet and infrared satellite sensors. Geochem Geophys Geosyst 2004;5(4):Q04001. doi:10.1029/2003GC000654. http://doi.wiley.com/10.1029/2003GC000654.

[103] Hall L.A., Anderson G.P. High-resolution solar spectrum between 2000 and 3100 å. J Geophys Res Atmos 96(D7):12927–12931. https://agupubs.onlinelibrary.wiley.com/doi/abs/10.1029/91JD01111. 10.1029/91JD01111.

[104] Harder JW, Brault JW. Atmospheric measurements of water vapor in the 442-nm region. J Geophys Res Atmos 1997;102(D5):6245–52. doi:10.1029/96JD01730. https://agupubs.onlinelibrary.wiley.com/doi/abs/10.1029/96JD01730.

[105] Hasekamp OP, Landgraf J. Ozone profile retrieval from backscattered ultraviolet radiances: the inverse problem solved by regularization. J Geophys Res Atmos 2001;106(D8):8077–88. doi:10.1029/2000JD900692. https://agupubs.onlinelibrary.wiley.com/doi/abs/10.1029/2000JD900692.

[106] Hausmann M, Platt U. Spectroscopic measurement of bromine oxide and ozone in the high arctic during polar sunrise experiment 1992. J Geophys Res Atmos 1994;99(D12):25399–413. doi:10.1029/94JD01314. https://agupubs.onlinelibrary.wiley.com/doi/abs/10.1029/94JD01314.

[107] Heath DF, Krueger AJ, Roeder HA, Henderson BD. The solar backscatter ultraviolet and total ozone mapping spectrometer (SBUV/TOMS) for NIMBUS g. Opt Eng 1975;14(4):14–149. doi:10.1117/12.7971839.

[108] Heath DF, Mateer CL, a K A R. The Nimbus-4 backscatter ultraviolet (BUV) atmospheric ozone experiment two years operation. Tech. Rep.. NASA Goddard Space Flight Center; 1973. https://ntrs.nasa.gov/search.jsp?R=19730010658.

[109] Hebestreit K, Stutz J, Rosen D, Matveiv V, Peleg M, Luria M, et al. DOAS measurements of tropospheric bromine oxide in mid-latitudes. Science 1999;283(5398):55–7. doi:10.1126/science.283.5398.55. http://science.sciencemag.org/content/283/5398/55.

[110] Hegels E, Crutzen PJ, Klüpfel T, Perner D, Burrows JP. Global distribution of atmospheric bromine-monoxide from GOME on earth observing satellite ERS-2. Geophys Res Lett 1998;25(16):3127–30. doi:10.1029/98GL02417. https://agupubs.onlinelibrary.wiley.com/doi/abs/10.1029/98GL02417.

[111] Herman JR, Cede A, Spinei E, Mount G, Tzortziou M, Abuhassan N. NO2 Column amounts from ground-based pandora and MFDOAS spectrometers using the direct-sun DOAS technique: intercomparisons and application to OMI validation. J Geophys Res 2009;114, D13307. doi:10.1029/2009JD011848. https://agupubs.onlinelibrary.wiley.com/doi/abs/10.1029/2009JD011848.

[112] Herman JR, Newman PA, McPeters R, Krueger AJ, Bhartia PK, Seftor CJ, et al. Meteor 3/total ozone mapping spectrometer observations of the 1993 ozone hole. J Geophys Res Atmos 1995;100(D2):2973–83. doi:10.1029/94JD02316. https://agupubs.onlinelibrary.wiley.com/doi/abs/10.1029/94JD02316.

[113] Heue K-P, Brenninkmeijer CAM, Baker AK, Rauthe-Schöch A, Walter D, Wagner T, et al. So2 and BrO observation in the plume of the eyjafjallajökull volcano 2010: CARIBIC and GOME-2 retrievals. Atmos Chem Phys 2011;11(6):2973–89. doi:10.5194/acp-11-2973-2011. https://www.atmos-chem-phys.net/11/2973/2011/.

[114] Hewson W, Barkley MP, González Abad G, Bösch H, Kurosu T, Spurr R, et al. Development and characterisation of a state-of-the-art GOME-2 formaldehyde air-mass factor algorithm. Atmos Meas Tech 2015;8(10):4055–74. doi:10.5194/amt-8-4055-2015. https://www.atmos-meas-tech.net/8/4055/2015/.

[115] Ho S-P, Peng L, Mears C, Anthes RA. Comparison of global observations and trends of total precipitable water derived from microwave radiometers and COSMIC radio occultation from 2006 to 2013. Atmos Chem Phys 2018;18(1):259–74. doi:10.5194/acp-18-259-2018. https://www.atmos-chem-phys.net/18/259/2018/.

[116] Holben BN, Eck TF, Slutsker I, Tanré D, Buis JP, Setzer A, et al. AERONET–A federated instrument network and data archive for aerosol characterization. Remote Sens Environ 1998;66(1):1–16. doi:10.1016/S0034-4257(98)00031-5. http://www.sciencedirect.com/science/article/pii/S0034425798000315.

[117] Hoogen R, Rozanov VV, Burrows JP. Ozone profiles from GOME satellite data: algorithm description and first validation. J Geophys Res Atmos 1999;104(D7):8263–80. doi:10.1029/1998JD100093. https://agupubs.onlinelibrary.wiley.com/doi/abs/10.1029/1998JD100093.

[118] Hörmann C, Sihler H, Beirle S, Penning de Vries M, Platt U, Wagner T. Seasonal variation of tropospheric bromine monoxide over the rann of kutch salt marsh seen from space. Atmos Chem Phys 2016;16(20):13015–34. doi:10.5194/acp-16-13015-2016. https://www.atmos-chem-phys.net/16/13015/2016/.

[119] Hörmann C, Sihler H, Bobrowski N, Beirle S, Penning de Vries M, Platt U, et al. Systematic investigation of bromine monoxide in volcanic plumes from space by using the GOME-2 instrument. Atmos Chem Phys 2013;13(9):4749–81. doi:10.5194/acp-13-4749-2013. https://www.atmos-chem-phys.net/13/4749/2013/.

[120] Huang F, Huang Y, Flynn LE, Wang W, Cao D, Wang S. Radiometric calibration of the solar backscatter ultraviolet sounder and validation of ozone profile retrievals. IEEE Trans Geosci Remote Sens 2012;50(12):4956–64. doi:10.1109/TGRS.2012.2211368.

[121] Hudman RC, Moore NE, Martin RV, Russell AR, Mebust AK, Valin LC, et al. A mechanistic model of global soil nitric oxide emissions: implementation and space based constraints. Atmos Chem Phys 2012;12:7779–95. doi:10.5194/acp-12-7779-2012. https://www.atmos-chem-phys.net/12/7779/2012/.

[122] Ingmann P, Veihelmann B, Langen J, Lamarre D, Stark H, Courrèges-Lacoste GB. Requirements for the GMES atmosphere service and ESA's implementation concept: sentinels-4/-5 and-5p. Remote Sens Environ 2012;120:58–69. doi:10.1016/j.rse.2012.01.023. http://www.sciencedirect.com/science/article/pii/S0034425712000673.

[123] Iozenas V. Determination of the vertical ozone distribution in the upper layers of the atmosphere from satellite measurements of ultraviolet solar radiation scattered by the Earth's atmosphere. Geomagn Aeron 1968;8:403–10.

[124] Irie H, Kanaya Y, Akimoto H, Iwabuchi H, Shimizu A, Aoki K. First retrieval of tropospheric aerosol profiles using MAX-DOAS and comparison with lidar and sky radiometer measurements. Atmos Chem Phys 2008;8(2):341–50. doi:10.5194/acp-8-341-2008. https://www.atmos-chem-phys.net/8/341/2008/acp-8-341-2008.html.

[125] Jin X, Fiore AM, Murray LT, Valin LC, Lamsal LN, Duncan B, et al. Evaluating a space-based indicator of surface ozone-NOx-VOC sensitivity over midlatitude source regions and application to decadal trends. J Geophys Res Atmos 2017;122(19):10,439–10,461. doi:10.1002/2017JD026720. https://agupubs.onlinelibrary.wiley.com/doi/abs/10.1002/2017JD026720.

[126] Jin X, Holloway T. Spatial and temporal variability of ozone sensitivity over china observed from the ozone monitoring instrument. J Geophys Res Atmos 2015;120(14):7229–46. doi:10.1002/2015JD023250. https://agupubs.onlinelibrary.wiley.com/doi/abs/10.1002/2015JD023250.

[127] Joiner J, Bhartia PK, Cebula RP, Hilsenrath E, McPeters RD, Park H. Rotational raman scattering (ring effect) in satellite backscatter ultraviolet measurements. Appl Opt 1995;34(21):4513–25. doi:10.1364/AO.34.004513. http://ao.osa.org/abstract.cfm?URI=ao-34-21-4513.

[128] Kaiser J, Wolfe GM, Min KE, Brown SS, Miller CC, Jacob DJ, et al. Reassessing the ratio of glyoxal to formaldehyde as an indicator of hydrocarbon precursor speciation. Atmos Chem Phys 2015;15(13):7571–83. doi:10.5194/acp-15-7571-2015. https://www.atmos-chem-phys.net/15/7571/2015/acp-15-7571-2015.html.

[129] Kar J, Fishman J, Creilson JK, Richter A, Ziemke J, Chandra S. Are there urban signatures in the tropospheric ozone column products derived from satellite measurements? Atmos Chem Phys 2010;10(11):5213–22. doi:10.5194/acp-10-5213-2010. https://www.atmos-chem-phys.net/10/5213/2010/.

[130] Kim J, Jeong U, Ahn MH, Kim JHKea. Geostationary environment monitoring spectrometer (GEMS): monitoring air quality from GEO in high temporal and spatial resolution over asia. Bull Am Meteorol Soc 2018;submitted.

[131] Kim SW, Heckel A, Frost GJ, Richter A, Gleason J, Burrows JP, et al. NO2 Columns in the Western United States observed from space and simulated by a regional chemistry model and their implications for NOx emissions. J Geophys Res 2009;114, D11301. doi:10.1029/2008JD011343. https://agupubs.onlinelibrary.wiley.com/doi/abs/10.1029/2008JD011343.

[132] Koukouli ME, Theys N, Ding J, Zyrichidou I, Mijling B, Balis D, et al. Updated SO2 emission estimates over china using OMI/aura observations. Atmos Meas Tech 2018;11(3):1817–32. doi:10.5194/amt-11-1817-2018. https://doi.org/10.5194/amt-11-1817-2018.

[133] Kramarova NA, Frith SM, Bhartia PK, McPeters RD, Taylor SL, Fisher BL, et al. Validation of ozone monthly zonal mean profiles obtained from the version 8.6 solar backscatter ultraviolet algorithm. Atmos Chem Phys 2013;13(14):6887–905. doi:10.5194/acp-13-6887-2013. https://www.atmos-chem-phys.net/13/6887/2013/.

[134] Krasnopolskii V. Ultraviolet spectrum of the radiation reflected by the Earth's atmosphere and its use in determining the total content and vertical distribution of atmospheric ozone (solar UV reflection and scattering from earth atmosphere, use in determining total concentration and vertical distribution of ozone). Geomagn Aeron 1966;6(2):236–42.

[135] Kromminga H, Orphal J, Spietz P, Voigt S, Burrows J. New measurements of OClo absorption cross-sections in the 325–435 nm region and their temperature dependence between 213 and 293 k. J Photochem Photo-

biol A 2003;157(2):149–60. doi:10.1016/S1010-6030(03)00071-6. http://www.sciencedirect.com/science/article/pii/S1010603003000716.

[136] Kroon M, de Haan JF, Veefkind JP, Froidevaux L, Wang R, Kivi R, et al. Validation of operational ozone profiles from the ozone monitoring instrument. J Geophys Res Atmos 2011;116(D18). doi:10.1029/2010JD015100. https://agupubs.onlinelibrary.wiley.com/doi/abs/10.1029/2010JD015100.

[137] Krotkov N, Carn S, Krueger A, Bhartia P, Yang K. Band residual difference algorithm for retrieval of SO$_2$ from the aura ozone monitoring instrument (OMI). IEEE Trans Geosci Remote Sens 2006;44(5):1259–66. doi:10.1109/TGRS.2005.861932. http://ieeexplore.ieee.org/xpls/abs_all.jsp?arnumber=1624604.

[138] Krotkov N, Habib S, da Silva A, Hughes E, Yang K, Brentzel K, et al. Real time volcanic cloud products and predictions for aviation alerts 6th AIAA atmospheric and space environments conference. American Institute of Aeronautics and Astronautics; 2014. doi:10.2514/6.2014-2618. http://arc.aiaa.org/doi/10.2514/6.2014-2618.

[139] Krotkov NA, McLinden CA, Li C, Lamsal LN, Celarier EA, Marchenko SV, et al. Aura OMI observations of regional SO$_2$ and NO$_2$ pollution changes from 2005 to 2015. Atmos Chem Phys 2016;16(7):4605–29. doi:10.5194/acp-16-4605-2016. https://www.atmos-chem-phys.net/16/4605/2016/.

[140] Krueger A. Sighting of el chichón sulfur dioxide clouds with the nimbus 7 total ozone mapping spectrometer. Science 1983;220(4604):1377–9. doi:10.1126/science.220.4604.1377. http://science.sciencemag.org/content/220/4604/1377.

[141] Krueger AJ, Heath DF, Mateer CL. Variations in the stratospheric ozone field inferred from nimbus satellite observations. Pure Appl Geophys 1973;106(1):1254–63. doi:10.1007/BF00881077.

[142] Krueger AJ, Schaefer SJ, Krotkov N, Bluth G, Barker S. Ultraviolet remote sensing of volcanic emissions. American Geophysical Union (AGU); 2013. p. 25–43. https://agupubs.onlinelibrary.wiley.com/doi/abs/10.1029/GM116p0025.

[143] Kuhn J, Platt U, Bobrowski N, Wagner T. Towards imaging of atmospheric trace gases using Fabry–Pérot interferometer correlation spectroscopy in the UV and visible spectral range. Atmos Meas Tech 2019;12(1):735–47. doi:10.5194/amt-12-735-2019. https://www.atmos-meas-tech.net/12/735/2019/.

[144] Kurosu TP, Chance K, Sioris CE. Preliminary results for HCHO and BrO from the EOS-Aura ozone monitoring instrument. In: Passive optical remote sensing of the atmosphere and clouds IV, 5652. SPIE; 2004. p. 116–24. doi:10.1117/12.578606. https://www.spiedigitallibrary.org/conference-proceedings-of-spie/5652/0000/Preliminary-results-for-HCHO-and-BrO-from-the-EOS-Aura/10.1117/12.578606.short.

[145] Kurtz MJ, Mink DJ, Wyatt WF, Fabricant DG, Torres G, Kriss GA, et al. XCSAO: a radial velocity package for the IRAF environment. In: Worrall DM, Biemesderfer C, Barnes J, editors. Astronomical data analysis software and systems I, ASP conf. ser., 25; 1992. p. 432–8.

[146] Kurucz RL, Furenlid I, Brault J, Testerman L. Solar flux atlas from 296 to 1300 nm, national solar observatory atlas, sunspot, new mexico: national solar observatory; 1984.

[147] Labow GJ, McPeters RD, Bhartia PK, Kramarova N. A comparison of 40 years of sbuv measurements of column ozone with data from the Dobson/Brewer network. J Geophys Res Atmos 2013;118(13):7370–8. doi:10.1002/jgrd.50503. https://agupubs.onlinelibrary.wiley.com/doi/abs/10.1002/jgrd.50503.

[148] Lamsal LN, Duncan BN, Yoshida Y, Krotkov NA, Pickering KE, Streets DG, et al. U.s. NO$_2$ trends: EPA air quality system (AQS) data versus improved observations from the ozone monitoring instrument (OMI). Atmos Environ 2015;110:130–43. doi:10.1016/j.atmosenv.2015.03.055. http://www.sciencedirect.com/science/article/pii/S1352231015002794.

[149] Lamsal LN, Martin RV, van Donkelaar A, Celarier EA, Bucsela EJ, Boersma KF, et al. Indirect validation of tropospheric nitrogen dioxide retrieved from the OMI satellite instrument: insight into the seasonal variation of nitrogen oxides at northern midlatitudes. J Geophys Res 2010;115, D05302. doi:10.1029/2009JD013351. https://agupubs.onlinelibrary.wiley.com/doi/abs/10.1029/2009JD013351.

[150] Lang R, Casadio S, Maurellis AN, Lawrence MG. Evaluation of the GOME water vapor climatology 1995–2002. J Geophys Res Atmos 2007;112(D17). doi:10.1029/2006JD008246. https://agupubs.onlinelibrary.wiley.com/doi/abs/10.1029/2006JD008246.

[151] Langley SP. The bolometer and radiant energy; 1881. Cambridge

[152] Langley SP, Abbot CG. Annals of the astrophysical observatory of the smithsonian institution; 1900. http://hdl.handle.net/2027/uva.x002221386.

[153] Lee C, Martin RV, van Donkelaar A, Lee H, Dickerson RR, Hains JC, et al. SO$_2$ Emissions and lifetimes: estimates from inverse modeling using in situ and global, space-based (SCIAMACHY and OMI) observations. J Geophys Res 2011;116(D6):D06304. doi:10.1029/2010JD014758. https://agupubs.onlinelibrary.wiley.com/doi/full/10.1029/2010JD014758.

[154] Lee C, Richter A, Weber M, Burrows JP. SO$_2$ Retrieval from SCIAMACHY using the weighting function DOAS (WFDOAS) technique: comparison with standard DOAS retrieval. Atmos Chem Phys 2008;8:6137–45. doi:10.5194/acp-8-6137-2008. https://doi.org/10.5194/acp-8-6137-2008.

[155] Lelieveld J, Dentener FJ. What controls tropospheric ozone? J Geophys Res Atmos 2000;105(D3):3531–51. doi:10.1029/1999JD901011. https://agupubs.onlinelibrary.wiley.com/doi/abs/10.1029/1999JD901011.

[156] Lerot C, Stavrakou T, De Smedt I, Müller J-F, Van Roozendael M. Glyoxal vertical columns from GOME-2 backscattered light measurements and comparisons with a global model. Atmos Chem Phys 2010;10(24):12059–72. doi:10.5194/acp-10-12059-2010. https://www.atmos-chem-phys.net/10/12059/2010/.

[157] Levelt PF, Joiner J, Tamminen J, Veefkind JP, Bhartia PK, Stein Zweers DC, et al. The ozone monitoring instrument: overview of 14 years in space. Atmos Chem Phys 2018;18(8):5699–745. doi:10.5194/acp-18-5699-2018. https://www.atmos-chem-phys.net/18/5699/2018/.

[158] Levelt PF, van der Oord GHJ, Dobber MR, Malkki A, Visser H, de Vries J, et al. The ozone monitoring instrument. IEEE Trans Geosci Remote Sens 2006;44(5):1093–101. doi:10.1109/TGRS.2006.872333.

[159] Li C, Joiner J, Krotkov NA, Bhartia PK. A fast and sensitive new satellite SO$_2$ retrieval algorithm based on principal component analysis: application to the ozone monitoring instrument. Geophys Res Lett 2013;40(23):6314–18. doi:10.1002/2013GL058134. http://doi.wiley.com/10.1002/2013GL058134.

[160] Li C, Joiner J, Krotkov NA, Dunlap L. A new method for global retrievals of HCHO total columns from the suomi national polar-orbiting partnership ozone mapping and profiler suite. Geophys Res Lett 2015;42. 2015GL063204, http://onlinelibrary.wiley.com/doi/10.1002/2015GL063204/abstract.

[161] Li C, Krotkov NA, Carn S, Zhang Y, Spurr RJD, Joiner J. New-generation NASA aura ozone monitoring instrument (OMI) volcanic SO$_2$ dataset: algorithm description, initial results, and continuation with the suomi-NPP ozone mapping and profiler suite (OMPS). Atmos Meas Tech 2017;10(2):445–58. doi:10.5194/amt-10-445-2017. https://www.atmos-meas-tech.net/10/445/2017/.

[162] Li C, McLinden C, Fioletov V, Krotkov N, Carn S, Joiner J, et al. India is overtaking china as the World's largest emitter of anthropogenic sulfur dioxide. Sci Rep 2017;7(1):14304. doi:10.1038/s41598-017-14639-8. http://www.nature.com/articles/s41598-017-14639-8.

[163] Li C, Zhang Q, Krotkov Na, Streets DG, He K, Tsay S-C, et al. Recent large reduction in sulfur dioxide emissions from chinese power plants observed by the ozone monitoring instrument. Geophys Res Lett 2010;37(8):L08807. doi:10.1029/2010GL042594. http://doi.wiley.com/10.1029/2010GL042594.

[164] Liu F, Choi S, Li C, Fioletov VE, McLinden CA, Joiner J, et al. A new global anthropogenic SO$_2$ emission inventory for the last decade: a mosaic of satellite-derived and bottom-up emissions. Atmos Chem Phys 2018;18(22):16571–86. doi:10.5194/acp-18-16571-2018. https://www.atmos-chem-phys.net/18/16571/2018/.

[165] Liu X, Bhartia PK, Chance K, Spurr RJD, Kurosu TP. Ozone profile retrievals from the ozone monitoring instrument. Atmos Chem Phys 2010;10(5):2521–37. doi:10.5194/acp-10-2521-2010. https://www.atmos-chem-phys.net/10/2521/2010/.

[166] Liu X, Chance K, Sioris CE, Spurr RJD, Kurosu TP, Martin RV, et al. Ozone profile and tropospheric ozone retrievals from the global ozone monitoring experiment: algorithm description and validation. J Geophys Res 2005;110(D20):D20307. doi:10.1029/2005JD006240. http://onlinelibrary.wiley.com/doi/10.1029/2005JD006240/abstract.

[167] Liu Y, Wang Y, Liu X, Cai Z, Chance K. Tibetan middle tropospheric ozone minimum in june discovered from GOME observations. Geophys Res Lett 2009;36(5). doi:10.1029/2008GL037056. https://agupubs.onlinelibrary.wiley.com/doi/abs/10.1029/2008GL037056.

[168] Llewellyn EJ, Lloyd ND, Degenstein DA, Gattinger RL, Petelina SV, Bourassa AE, et al. The OSIRIS instrument on the odin spacecraft. Can J Phys 2004;82(6):411–22. doi:10.1139/p04-005.

[169] Lorente A, Folkert Boersma K, Yu H, Dörner S, Hilboll A, Richter A, et al. Structural uncertainty in air mass factor calculation for NO$_2$ and HCHO satellite retrievals. Atmos Meas Tech 2017;10(3):759–82. doi:10.5194/amt-10-759-2017. https://www.atmos-meas-tech.net/10/759/2017/.

[170] Lu Z, Streets DG. Increase in NO$_x$ emissions from indian thermal power plants during 1996–2010: unit-based inventories and multisatellite observations. Environ Sci Technol 2012;46(14):7463–70. doi:10.1021/es300831w. https://doi.org/10.1021/es300831w.

[171] Lu Z, Streets DG, de Foy B, Lamsal LN, Duncan BN, Xing J. Emissions of nitrogen oxides from US urban areas: estimation from ozone monitoring instrument retrievals for 2005–2014. Atmos Chem Phys 2015;15:10367–83. doi:10.5194/acp-15-10367-2015. https://www.atmos-chem-phys.net/15/10367/2015/.

[172] Lu Z, Zhang Q, Streets DG. Sulfur dioxide and primary carbonaceous aerosol emissions in china and india, 1996–2010. Atmos Chem Phys 2011;11(18):9839–64. doi:10.5194/acp-11-9839-2011. http://www.atmos-chem-phys.net/11/9839/2011/.

[173] Malicet J, Daumont D, Charbonnier J, Parisse C, Chakir A, Brion J. Ozone UV spectroscopy. II. absorption cross-sections and temperature dependence. J Atmos Chem 1995;21(3):263–73. doi:10.1007/BF00696758. https://doi.org/10.1007/BF00696758.

[174] Marais EA, Jacob DJ, Kurosu TP, Chance K, Murphy JG, Reeves C, et al. Isoprene emissions in africa inferred from OMI observations of formaldehyde columns. Atmos Chem Phys 2012;12(14):6219–35. doi:10.5194/acp-12-6219-2012. https://www.atmos-chem-phys.net/12/6219/2012.html.

[175] Marchenko S, Krotkov NA, Lamsal LN, Celarier EA, Swartz WH, Bucsela EJ. Revising the slant column density retrieval of nitrogen dioxide observed by the ozone monitoring instrument. J Geophys Res Atmos 2015;120(11):5670–92. doi:10.1002/2014JD022913. https://agupubs.onlinelibrary.wiley.com/doi/abs/10.1002/2014JD022913.

[176] Maresi L, Van Der Meulen W, Vink R. TROPOLITE, on the path of atmospheric chemistry made simple. In: Sensor, systems, and next-generation satellites XVIII, 9241; 2014. p. 9241–52. doi:10.1117/12.2067473.

[177] Marshak A, Herman J, Adam S, Karin B, Carn S, Cede A, et al. Earth observations from DSCOVR EPIC instrument. Bull Am Meteorol Soc 2018;99(9):1829–50. doi:10.1175/BAMS-D-17-0223.1. https://doi.org/10.1175/BAMS-D-17-0223.1.

[178] Martin RV. Satellite remote sensing of surface air quality. Atmos Environ 2008;42(34):7823–43. doi:10.1016/j.atmosenv.2008.07.018. http://www.sciencedirect.com/science/article/pii/S1352231008006328.

[179] Martin RV, Chance K, Jacob DJ, et al. An improved retrieval of tropospheric nitrogen dioxide from GOME. J Geophys Res 2002;107. doi:10.1029/2001JD001027. https://agupubs.onlinelibrary.wiley.com/doi/abs/10.1029/2001JD001027.

[180] Martin JCG, Spietz P, Burrows JP. Spectroscopic studies of the i_2/o_3 photochemistry: part 1: determination of the absolute absorption cross sections of iodine oxides of atmospheric relevance. J Photochem Photobiol A 2005;176(1):15–38. doi:10.1016/j.jphotochem.2005.09.024. http://www.sciencedirect.com/science/article/pii/S1010603005004661.

[181] McCormick MP, Thomason LW, Trepte CR. Atmospheric effects of the Mt Pinatubo eruption. Nature 1995;373(6513):399–404. doi:10.1038/373399a0. https://www.nature.com/articles/373399a0.

[182] McLinden CA, Fioletov V, Shephard MW, Krotkov N, Li C, Martin RV, et al. Space-based detection of missing sulfur dioxide sources of global air pollution. Nature Geosci 2016;9(7):496–500. doi:10.1038/ngeo2724. http://www.nature.com/articles/ngeo2724.

[183] McPeters RD. The atmospheric SO_2 budget for pinatubo derived from noaa-11 SBUV/2 spectral data. Geophys Res Lett 1993;20(18):1971–4. doi:10.1029/93GL02360. http://doi.wiley.com/10.1029/93GL02360.

[184] McPeters RD, Bhartia PK, Haffner D, Labow GJ, Flynn L. The version 8.6 SBUV ozone data record: an overview. J Geophys Res Atmos 2013;118(14):8032–9. doi:10.1002/jgrd.50597.

[185] McPeters RD, Heath DF, Schlesinger BM. Satellite observation of SO_2 from El Chichón: identification and measurement. Geophys Res Lett 1984;11(12):1203–6. doi:10.1029/GL011i012p01203. http://doi.wiley.com/10.1029/GL011i012p01203.

[186] McPeters RD, Labow GJ, Logan JA. Ozone climatological profiles for satellite retrieval algorithms. J Geophys Res Atmos 2007;112(D5). doi:10.1029/2005JD006823. https://agupubs.onlinelibrary.wiley.com/doi/abs/10.1029/2005JD006823.

[187] Mears CA, Smith DK, Ricciardulli L, Wang J, Huelsing H, Wentz FJ. Construction and uncertainty estimation of a satellite-derived total precipitable water data record over the world's oceans. Earth Space Sci 2018;5(5):197–210. doi:10.1002/2018EA000363. https://agupubs.onlinelibrary.wiley.com/doi/abs/10.1002/2018EA000363.

[188] Mears CA, Smith DK, Wentz FJ. Estimated errors in retrievals of ocean parameters from SSMIS. J Geophys Res Atmos 2015;120(12):5816–30. doi:10.1002/2014JD023049. https://agupubs.onlinelibrary.wiley.com/doi/abs/10.1002/2014JD023049.

[189] Mears CA, Wang J, Smith D, Wentz FJ. Intercomparison of total precipitable water measurements made by satellite-borne microwave radiometers and ground-based GPS measurements. J Geophys Res Atmos 2015;120(6):2492–504. doi:10.1002/2014JD022694. https://agupubs.onlinelibrary.wiley.com/doi/abs/10.1002/2014JD022694.

[190] Meller R, Moortgat GK. Temperature dependence of the absorption cross sections of formaldehyde between 223 and 323 k in the wavelength range 225–375 nm. J Geophys Res Atmos 2000;105(D6):7089–101. doi:10.1029/1999JD901074. https://agupubs.onlinelibrary.wiley.com/doi/abs/10.1029/1999JD901074.

[191] Miles GM, Siddans R, Kerridge BJ, Latter BG, Richards NAD. Tropospheric ozone and ozone profiles retrieved from GOME-2 and their validation. Atmos Meas Tech 2015;8(1):385–98. doi:10.5194/amt-8-385-2015. https://www.atmos-meas-tech.net/8/385/2015/.

[192] Millet DB, Jacob DJ, Boersma KF, Fu T-M, Kurosu TP, Chance K, et al. Spatial distribution of isoprene emissions from North America derived from formaldehyde column measurements by the OMI satellite sensor. J Geophys Res Atmos 2008;113(D2). doi:10.1029/2007JD008950. https://agupubs.onlinelibrary.wiley.com/doi/abs/10.1029/2007JD008950.

[193] Millet DB, Jacob DJ, Turquety S, Hudman RC, Wu S, Fried A, et al. Formaldehyde distribution over North America: implications for satellite retrievals of formaldehyde columns and isoprene emission. J Geophys Res Atmos 2006;111(D24). doi:10.1029/2005JD006853. https://agupubs.onlinelibrary.wiley.com/doi/abs/10.1029/2005JD006853.

[194] Müller MD, Kaifel AK, Weber M, Tellmann S, Burrows JP, Loyola D. Ozone profile retrieval from global ozone monitoring experiment (GOME) data using a neural network approach (neural network ozone retrieval system (NNORSY)). J Geophys Res Atmos 2003;108(D16). doi:10.1029/2002JD002784. https://agupubs.onlinelibrary.wiley.com/doi/abs/10.1029/2002JD002784.

[195] Munro R, Lang R, Klaes D, Poli G, Retscher C, Lindstrot R, et al. The GOME-2 instrument on the metop series of satellites: instrument design, calibration, and level 1 data processing an overview. Atmos Meas Tech 2016;9(3):1279–301. doi:10.5194/amt-9-1279-2016. https://www.atmos-meas-tech.net/9/1279/2016/.

[196] Munro R, Siddans R, Reburn WJ, Kerridge BJ. Direct measurement of tropospheric ozone distributions from space. Nature 1998;392:168–71. doi:10.1038/32392. https://doi.org/10.1038/32392.

[197] Myhre G, Shindell D, Bréon F-M, Collins W, Fuglestvedt J, Huang J, et al. Anthropogenic and natural radiative forcing. In: Climate change 2013: the physical science basis contribution of working group I to the fifth assessment report of the intergovernmental panel on climate change; 2013. p. 659–740. doi:10.1017/CBO9781107415324.018.

[198] Nelson RR, Crisp D, Ott LE, O'Dell CW. High-accuracy measurements of total column water vapor from the orbiting carbon observatory-2. Geophys Res Lett 2016;43(23):12,261–12,269. doi:10.1002/2016GL071200. https://agupubs.onlinelibrary.wiley.com/doi/abs/10.1002/2016GL071200.

[199] Niemeier U, Timmreck C. What is the limit of climate engineering by stratospheric injection of SO_2? Atmos Chem Phys 2015;15(16):9129–41. doi:10.5194/acp-15-9129-2015. https://www.atmos-chem-phys.net/15/9129/2015/.

[200] Ning T, Wang J, Elgered G, Dick G, Wickert J, Bradke M, et al. The uncertainty of the atmospheric integrated water vapour estimated from GNSS observations. Atmos Meas Tech 2016;9(1):79–92. doi:10.5194/amt-9-79-2016. https://www.atmos-meas-tech.net/9/79/2016/.

[201] Noël S, Buchwitz M, Bovensmann H, Hoogen R, Burrows JP. Atmospheric water vapor amounts retrieved from GOME satellite data. Geophys Res Lett 1999;26(13):1841–4. doi:10.1029/1999GL900437. https://agupubs.onlinelibrary.wiley.com/doi/abs/10.1029/1999GL900437.

[202] Noël S, Buchwitz M, Burrows JP. First retrieval of global water vapour column amounts from SCIAMACHY measurements. Atmos Chem Phys 2004;4(1):111–25. doi:10.5194/acp-4-111-2004. https://www.atmos-chem-phys.net/4/111/2004/.

[203] Nowlan CR, Liu X, Chance K, Cai Z, Kurosu TP, Lee C, et al. Retrievals of sulfur dioxide from the global ozone monitoring experiment 2 (GOME-2) using an optimal estimation approach: algorithm and initial validation. J Geophys Res 2011;116(D18):D18301. doi:10.1029/2011JD015808. https://agupubs.onlinelibrary.wiley.com/doi/full/10.1029/2011JD015808.

[204] Nowlan CR, Martin RV, Philip S, Lamsal LN, Krotkov NA, Marais EA, et al. Global dry deposition of nitrogen dioxide and sulfur dioxide inferred from space-based measurements. Glob Biogeochem Cycles 2014;28(10):1025–43. doi:10.1002/2014GB004805. https://agupubs.onlinelibrary.wiley.com/doi/abs/10.1002/2014GB004805.

[205] Palmer PI, Abbot DS, Fu T-M, Jacob DJ, Chance K, Kurosu TP, et al. Quantifying the seasonal and interannual variability of North American isoprene emissions using satellite observations of the formaldehyde column. J Geophys Res Atmos 2006;111(D12). doi:10.1029/2005JD006689. https://agupubs.onlinelibrary.wiley.com/doi/abs/10.1029/2005JD006689.

[206] Palmer PI, Jacob DJ, Chance K, Martin RV, Spurr RJD, Kurosu TP, et al. Air mass factor formulation for spectroscopic measurements from satellites: application to formaldehyde retrievals from the global ozone monitoring experiment. J Geophys Res Atmos 2001;106(D13):14539–50. doi:10.1029/2000JD900772. https://agupubs.onlinelibrary.wiley.com/doi/abs/10.1029/2000JD900772.

[207] Pan C, Weng F, Flynn L. Spectral performance and calibration of the suomi NPP OMPS nadir profiler sensor. Earth Space Sci 2017;4(12):737–45. doi:10.1002/2017EA000336. https://agupubs.onlinelibrary.wiley.com/doi/abs/10.1002/2017EA000336.

[208] Pawson S, Steinbrecht W, Charlton-Perez A, Fujiwara M, Karpechko A, Petropavlovskikh I, et al. Update on global ozone: past, present, and future, chapter 2 in scientific assessment of ozone depletion: 2014 Tech. Rep. 55. Geneva, Switzerland: World Meteorological Organization; 2014. https://www.wmo.int/pages/prog/arep/gaw/ozone_2014/full_report_TOC.html.

[209] Pérez-Ramírez D, Whiteman DN, Smirnov A, Lyamani H, Holben BN, Pinker R, et al. Evaluation of aeronet precipitable water versus microwave radiometry, gps, and radiosondes at arm sites. J Geophys Res Atmos 2014;119(15):9596–613. doi:10.1002/2014JD021730. https://agupubs.onlinelibrary.wiley.com/doi/abs/10.1002/2014JD021730.

[210] Piesanie Ad, Piters AJM, Aben I, Schrijver H, Wang P, Noël S. Validation of two independent retrievals of SCIAMACHY water vapour columns using radiosonde data. Atmos Meas Tech 2013;6(10):2925–40. doi:10.5194/amt-6-2925-2013. https://www.atmos-meas-tech.net/6/2925/2013/.

[211] Platt U. Differential optical absorption spectroscopy, air monitoring. Am Cancer Soc; 2006. ISBN 9780470027318. https://onlinelibrary.wiley.com/doi/abs/10.1002/9780470027318.a0706.

[212] Platt U, Wagner T. Satellite mapping of enhanced BrO concentrations in the troposphere. Nature 1998;395(6701):486–90. doi:10.1038/26723. https://www.nature.com/articles/26723.

[213] Pope CA, Dockery DW. Health effects of fine particulate air pollution: lines that connect. J Air Waste Manag Assoc 2006;56(6):709–42. doi:10.1080/10473289.2006.10464485. https://www.tandfonline.com/doi/full/10.1080/10473289.2006.10464485.

[214] Pope RJ, Chipperfield MP, Savage NH, Ordonez C, Neal LS, Lee LA, et al. Evaluation of a regional air quality model using satellite column NO_2: treatment of observation errors and model boundary conditions and emissions. Atmos Chem Phys 2015;15:5611–26. doi:10.5194/acp-15-5611-2015. https://www.atmos-chem-phys.net/15/5611/2015/.

[215] Rasool QZ, Zhang R, Lash B, Cohan DS, Cooter E, Bash J, et al. Enhanced representation of soil NO emissions in the community multiscale air quality (CMAQ) model version 5.0.2. Geosci Model Dev 2016;9:3177–97. doi:10.5194/gmd-9-3177-2016. https://www.geosci-model-dev.net/9/3177/2016/.

[216] Rawcliffe RD, Elliott DD. Latitude distribution of ozone at high altitudes, deduced from a satellite measurement of the earth's radiance at 2840 a. J Geophys Res 1966;71(21):5077–89. doi:10.1029/JZ071i021p05077. https://agupubs.onlinelibrary.wiley.com/doi/abs/10.1029/JZ071i021p05077.

[217] Richter A, Begoin M, Hilboll A, Burrows JP. An improved NO_2 retrieval for the GOME-2 satellite instrument. Atmos Meas Tech 2011;4:1147–59. doi:10.5194/amt-4-1147-2011. https://www.atmos-meas-tech.net/4/1147/2011/.

[218] Richter A, Wittrock F, Eisinger M, Burrows JP. GOME observations of tropospheric BrO in northern hemispheric spring and summer 1997. Geophys Res Lett 1998;25(14):2683–6. doi:10.1029/98GL52016. https://agupubs.onlinelibrary.wiley.com/doi/abs/10.1029/98GL52016.

[219] Richter D, Weibring P, Walega JG, Fried A, Spuler SM, Taubman MS. Compact highly sensitive multi-species airborne mid-IR spectrometer. Appl Phys B 2015;119(1):119–31. doi:10.1007/s00340-015-6038-8. https://doi.org/10.1007/s00340-015-6038-8.

[220] Rix M, Valks P, Hao N, Loyola D, Schlager H, Huntrieser H, et al. Volcanic SO_2, BrO and plume height estimations using GOME-2 satellite measurements during the eruption of eyjafjallajökull in may 2010. J Geophys Res Atmos 2012;117(6):1–19. doi:10.1029/2011JD016718. https://agupubs.onlinelibrary.wiley.com/doi/abs/10.1029/2011JD016718.

[221] Rodgers CD. Inverse methods for atmospheric sounding. World Scientific; 2000. doi:10.1142/3171. https://www.worldscientific.com/doi/abs/10.1142/3171.

[222] Saiz-Lopez A, Chance K, Liu X, Kurosu TP, Sander SP. First observations of iodine oxide from space. Geophys Res Lett 2007;34(12). doi:10.1029/2007GL030111. https://agupubs.onlinelibrary.wiley.com/doi/abs/10.1029/2007GL030111.

[223] Salawitch RJ, Canty T, Kurosu T, Chance K, Liang Q, da Silva A, et al. A new interpretation of total column bro during arctic spring. Geophys Res Lett 2010;37(21). doi:10.1029/2010GL043798. https://agupubs.onlinelibrary.wiley.com/doi/abs/10.1029/2010GL043798.

[224] Salawitch RJ, Weisenstein DK, Kovalenko LJ, Sioris CE, Wennberg PO, Chance K, et al. Sensitivity of ozone to bromine in the lower stratosphere. Geophys Res Lett 2005;32(5). doi:10.1029/2004GL021504. https://agupubs.onlinelibrary.wiley.com/doi/abs/10.1029/2004GL021504.

[225] Sander S, Bekker D, Blavier J-F, Bryk M, Donahue C, Goullioud R, et al. Panchromatic Fourier transform spectrometer engineering model (PanFTS-EM) for geostationary atmospheric measurements. In: Fourier transform spectroscopy and hyperspectral imaging and sounding of the environment. Optical Society of America; 2015. p. FW4A.2. doi:10.1364/FTS.2015.FW4A.2. http://www.osapublishing.org/abstract.cfm?URI=FTS-2015-FW4A.2.

[226] Sauvage B, Martin RV, van Donkelaar A, Liu X, Chance K, Jaeglé L, et al. Remote sensed and in situ constraints on processes affecting tropical tropospheric ozone. Atmos Chem Phys 2007;7(3):815–38. doi:10.5194/acp-7-815-2007. https://www.atmos-chem-phys.net/7/815/2007/.

[227] Schenkeveld VME, Jaross G, Marchenko S, Haffner D, Kleipool QL, Rozemeijer NC, et al. In-flight performance of the ozone monitoring instrument. Atmos Meas Tech 2017;10:1957–86. https://www.atmos-meas-tech.net/10/1957/2017/.

[228] Schröder M, Lockhoff M, Fell F, Forsythe J, Trent T, Bennartz R, et al. The GEWEX water vapor assessment archive of water vapour products from satellite observations and reanalyses. Earth Syst Sci Data 2018;10(2):1093–117. doi:10.5194/essd-10-1093-2018. https://www.earth-syst-sci-data.net/10/1093/2018/.

[229] Seftor CJ, Jaross G, Kowitt M, Haken M, Li J, Flynn LE. Postlaunch performance of the suomi national polar-orbiting partnership ozone mapping and profiler suite (OMPS) nadir sensors. J Geophys Res Atmos 2014;119(7):4413–28. doi:10.1002/2013JD020472. https://agupubs.onlinelibrary.wiley.com/doi/abs/10.1002/2013JD020472.

[230] Seidel DJ, Berger FH, Diamond HJ, Dykema J, Goodrich D, Immler F, et al. Reference upper-air observations for climate: rationale, progress, and plans. Bull Am Meteorol Soc 2009;90(3):361–9. doi:10.1175/2008BAMS2540.1. https://journals.ametsoc.org/doi/10.1175/2008BAMS2540.1.

[231] Seo S, Richter A, Blechschmidt A-M, Bougoudis I, Burrows JP. First high resolution BrO column retrievals from TROPOMI. Atmos Meas Tech Discuss 2018;2018:1–26. doi:10.5194/amt-2018-365. https://www.atmos-meas-tech-discuss.net/amt-2018-365/.

[232] Serdyuchenko A, Gorshelev V, Weber M, Chehade W, Burrows JP. High spectral resolution ozone absorption cross-sections – part 2: temperature dependence. Atmos Meas Tech 2014;7(2):625–36. doi:10.5194/amt-7-625-2014. https://www.atmos-meas-tech.net/7/625/2014/.

[233] Shim C, Wang Y, Choi Y, Palmer PI, Abbot DS, Chance K. Constraining global isoprene emissions with global ozone monitoring experiment (GOME) formaldehyde column measurements. J Geophys Res Atmos 2005;110(D24). doi:10.1029/2004JD005629. https://agupubs.onlinelibrary.wiley.com/doi/full/10.1029/2004JD005629.

[234] Silva S.J., Heald C.L., Li M. Space-based constraints on terrestrial glyoxal production. J Geophys Res Atmos; 123(23):13,583–13,594. https://agupubs.onlinelibrary.wiley.com/doi/abs/10.1029/2018JD029311. 10.1029/2018JD029311.

[235] Simpson WR, Brown SS, Saiz-Lopez A, Thornton JA, von Glasow R. Tropospheric halogen chemistry: sources, cycling, and impacts. Chem Rev 2015;115(10):4035–62. doi:10.1021/cr5006638.

[236] Simpson WR, von Glasow R, Riedel K, Anderson P, Ariya P, Bottenheim J, et al. Halogens and their role in polar boundary-layer ozone depletion. Atmos Chem Phys 2007;7(16):4375–418. doi:10.5194/acp-7-4375-2007. https://www.atmos-chem-phys.net/7/4375/2007/.

[237] Singer SF, Wentworth RC. A method for the determination of the vertical ozone distribution from a satellite. J Geophys Res 1957;62(2):299–308. doi:10.1029/JZ062i002p00299. https://agupubs.onlinelibrary.wiley.com/doi/abs/10.1029/JZ062i002p00299.

[238] Solomon S, Ivy DJ, Kinnison D, Mills MJ, Neely RR, Schmidt A. Emergence of healing in the antarctic ozone layer. Science 2016;353(6296):269–74. doi:10.1126/science.aae0061. http://science.sciencemag.org/content/353/6296/269.

[239] Souri AH, Choi Y, Jeon W, Woo J-H, Zhang Q, Kurokawa J-i. Remote sensing evidence of decadal changes in major tropospheric ozone precursors over east asia. J Geophys Res Atmos 2017;122(4):2474–92.

[240] Spinei E, Whitehill A, Fried A, Tiefengraber M, Knepp TN, Herndon S, et al. The first evaluation of formaldehyde column observations by improved pandora spectrometers during the korus-aq field study. Atmos Meas Tech 2018;11(9):4943–61. doi:10.5194/amt-11-4943-2018. https://www.atmos-meas-tech.net/11/4943/2018/.

[241] Stavrakou T, Müller J-F, De Smedt I, Van Roozendael M, Kanakidou M, Vrekoussis M, et al. The continental source of glyoxal estimated by the synergistic use of spaceborne measurements and inverse modelling. Atmos Chem Phys 2009;9(21):8431–46. doi:10.5194/acp-9-8431-2009. https://www.atmos-chem-phys.net/9/8431/2009/.

[242] Stavrakou T, Müller J-F, De Smedt I, Van Roozendael M, van der Werf GR, Giglio L, et al. Evaluating the performance of pyrogenic and biogenic emission inventories against one decade of space-based formaldehyde columns. Atmos Chem Phys 2009;9(3):1037–60. doi:10.5194/acp-9-1037-2009. https://www.atmos-chem-phys.net/9/1037/2009/acp-9-1037-2009.html.

[243] Stavrakou T, Müller J-F, De Smedt I, Van Roozendael M, van der Werf GR, Giglio L, et al. Global emissions of non-methane hydrocarbons deduced from SCIAMACHY formaldehyde columns through 2003–2006. Atmos Chem Phys 2009;9(11):3663–79. doi:10.5194/acp-9-3663-2009. https://www.atmos-chem-phys.net/9/3663/2009/acp-9-3663-2009.html.

[244] Suleiman RM, Chance K, Liu X, González Abad G, Kurosu TP, Hendrick F, et al. OMI Total bromine monoxide (OMBRO) data product: algorithm, retrieval and measurement comparisons. Atmos Meas Tech 2019;12(4):2067–84. doi:10.5194/amt-12-2067-2019. https://www.atmos-meas-tech.net/12/2067/2019/.

[245] Thalman R, Volkamer R. Temperature dependent absorption cross-sections of o_2-o_2 collision pairs between 340 and 630 nm and at atmospherically relevant pressure. Phys Chem Chem Phys 2013;15:15371–81. doi:10.1039/C3CP50968K. https://doi.org/10.1039/C3CP50968K.

[246] Theys N, Campion R, Clarisse L, Brenot H, van Gent J, Dils B, et al. Volcanic SO_2 fluxes derived from satellite data: a survey using OMI, GOME-2, IASI and MODIS. Atmos Chem Phys 2013;13(12):5945–68. doi:10.5194/acp-13-5945-2013. https://www.atmos-chem-phys.net/13/5945/2013/.

[247] Theys N, De Smedt I, van Gent J, Danckaert T, Wang T, Hendrick F, et al. Sulfur dioxide vertical column DOAS retrievals from the ozone monitoring instrument: global observations and comparison to ground-based and satellite data. J Geophys Res Atmos 2015;120:2470–91. doi:10.1002/2014JD022657. https://agupubs.onlinelibrary.wiley.com/doi/abs/10.1002/2014JD022657.

[248] Theys N, De Smedt I, Yu H, Danckaert T, van Gent J, Hörmann C, et al. Sulfur dioxide retrievals from TROPOMI onboard sentinel-5 precursor: algorithm theoretical basis. Atmos Meas Tech 2017;10(1):119–53. doi:10.5194/amt-10-119-2017. https://www.atmos-meas-tech.net/10/119/2017/.

[249] Theys N, Van Roozendael M, Dils B, Hendrick F, Hao N, De Maziére M. First satellite detection of volcanic bromine monoxide emission after the kasatochi eruption. Geophys Res Lett 2009;36(3). doi:10.1029/2008GL036552. https://agupubs.onlinelibrary.wiley.com/doi/abs/10.1029/2008GL036552.

[250] Thuillier G, Hersé M, Labs D, Foujols T, Peetermans W, Gillotay D, et al. The solar spectral irradiance from 200 to 2400 nm as measured by the SOLSPEC spectrometer from the atlas and eureca missions. Sol Phys 2003;214:1–22. doi:10.1023/A:1024048429145. https://doi.org/10.1023/A:1024048429145.

[251] Tong D, Lamsal LN, Pan L, Kim H, Lee P, Chai T, et al. Long-term NO_x trends over large cities in the united states: comparison of satellite retrievals, ground observations, and emission inventories. Atmos Environ 2015;107:70–84. doi:10.1016/j.atmosenv.2015.01.035. http://www.sciencedirect.com/science/article/pii/S1352231015000564.

[252] Toyota K, McConnell JC, Lupu A, Neary L, McLinden CA, Richter A, et al. Analysis of reactive bromine production and ozone depletion in the arctic boundary layer using 3-D simulations with GEM-AQ: inference from synoptic-scale patterns. Atmos Chem Phys 2011;11(8):3949–79. doi:10.5194/acp-11-3949-2011. https://www.atmos-chem-phys.net/11/3949/2011/.

[253] Valin LC, Fiore AM, Chance K, González Abad G. The role of OH production in interpreting the variability of CH_2O columns in the southeast u.s.. J Geophys Res Atmos 2016;121(1):478–93. doi:10.1002/2015JD024012. https://agupubs.onlinelibrary.wiley.com/doi/abs/10.1002/2015JD024012.

[254] Valks P, Pinardi G, Richter A, Lambert JC, Hao N, Loyola D, et al. Operational total and tropospheric NO_2 column retrieval for GOME-2. Atmos Meas Tech 2011;4:1491–514. doi:10.5194/amt-4-1491-2011. https://www.atmos-meas-tech.net/4/1491/2011/.

[255] van der A RJ, van Oss RF, Piters AJM, Fortuin JPF, Meijer YJ, Kelder HM. Ozone profile retrieval from recalibrated global ozone monitoring experiment data. J Geophys Res Atmos 2002;107(D15). doi:10.1029/2001JD000696. https://agupubs.onlinelibrary.wiley.com/doi/abs/10.1029/2001JD000696.

[256] van Peet JCA, van der A RJ, Tuinder ONE, Wolfram E, Salvador J, Levelt PF, et al. Ozone profile retrieval algorithm (OPERA) for nadir-looking satellite instruments in the UVVIS. Atmos Meas Tech 2014;7(3):859–76. doi:10.5194/amt-7-859-2014. https://www.atmos-meas-tech.net/7/859/2014/.

[257] van Roozendael M, de Smedt I, Fayt C, Wittrock F, Richter A, Afe O. First validation of SCIAMACHY BrO columns. Atmospheric chemistry validation of ENVISAT (ACVE-2), 562; 2004.

[258] Vandaele A, Hermans C, Simon P, Carleer M, Colin R, Fally S, et al. Measurements of the NO_2 absorption cross-section from 42000 cm^1 to 10000 cm^1 (2381000 nm) at 220 k and 294 k. J Quant Spectrosc Radiat Transf 1998;59(3):171–84. doi:10.1016/S0022-4073(97)00168-4. http://www.sciencedirect.com/science/article/pii/S0022407397001684.

[259] Vasilkov AP, Joiner J, Gleason J, Bhartia PK. Ocean raman scattering in satellite backscatter UV measurements. Geophys Res Lett 2002;29(17):18–1–18–4. doi:10.1029/2002GL014955.

[260] Veefkind JP, Aben I, McMullan K, Förster H, de Vries J, Otter G, et al. TROPOMI On the ESA sentinel-5 precursor: a GMES mission for global observations of the atmospheric composition for climate, air quality and ozone layer applications. Remote Sens Environ 2012;120:70–83. doi:10.1016/j.rse.2011.09.027. http://www.sciencedirect.com/science/article/pii/S0034425712000661.

[261] Venkateswaran SV, Moore JG, Krueger AJ. Determination of the vertical distribution of ozone by satellite photometry. J Geophys Res 1961;66(6):1751–71. doi:10.1029/JZ066i006p01751. https://agupubs.onlinelibrary.wiley.com/doi/abs/10.1029/JZ066i006p01751.

[262] Vigouroux C, Aquino B, Augusto C, Bauwens M, Becker C, Blumenstock T, et al. NDACC Harmonized formaldehyde time series from 21 FTIR stations covering a wide range of column abundances. Atmos Meas Tech 2018;11(9):5049–73. doi:10.5194/amt-11-5049-2018. https://www.atmos-meas-tech.net/11/5049/2018/amt-11-5049-2018.html.

[263] Vigouroux C, Hendrick F, Stavrakou T, Dils B, De Smedt I, Hermans C, et al. Ground-based FTIR and MAX-DOAS observations of formaldehyde at réunion island and comparisons with satellite and model data. Atmos Chem Phys 2009;9(24):9523–44. doi:10.5194/acp-9-9523-2009. https://www.atmos-chem-phys.net/9/9523/2009/.

[264] Volkamer R, Molina LT, Molina MJ, Shirley T, Brune WH. DOAS Measurement of glyoxal as an indicator for fast voc chemistry in urban air. Geophys Res Lett 2005;32(8). doi:10.1029/2005GL022616. https://agupubs.onlinelibrary.wiley.com/doi/abs/10.1029/2005GL022616.

[265] Volkamer R, Spietz P, Burrows J, Platt U. High-resolution absorption cross-section of glyoxal in the UV–vis and IR spectral ranges. J Photochem Photobiol A 2005;172(1):35–46. doi:10.1016/j.jphotochem.2004.11.011. http://www.sciencedirect.com/science/article/pii/S1010603004005143.

[266] von Glasow R, von Kuhlmann R, Lawrence MG, Platt U, Crutzen PJ. Impact of reactive bromine chemistry in the troposphere. Atmos Chem Phys 2004;4(11/12):2481–97. doi:10.5194/acp-4-2481-2004. https://www.atmos-chem-phys.net/4/2481/2004/.

[267] Vountas M, Rozanov V, Burrows J. Ring effect: impact of rotational raman scattering on radiative transfer in earth's atmosphere. J Quant Spectrosc Radiat Transf 1998;60(6):943–61. doi:10.1016/S0022-4073(97)00186-6. http://www.sciencedirect.com/science/article/pii/S0022407397001866.

[268] Vrekoussis M, Wittrock F, Richter A, Burrows JP. GOME-2 Observations of oxygenated VOCs: what can we learn from the ratio glyoxal to formaldehyde on a global scale? Atmos Chem Phys 2010;10(21):10145–60. doi:10.5194/acp-10-10145-2010. https://www.atmos-chem-phys.net/10/10145/2010/.

[269] Wagner T, Beirle S, Sihler H, Mies K. A feasibility study for the retrieval of the total column precipitable water vapour from satellite observations in the blue spectral range. Atmos Meas Tech 2013;6(10):2593–605. doi:10.5194/amt-6-2593-2013. https://www.atmos-meas-tech.net/6/2593/2013/.

[270] Wagner T, Heland J, Zöger M, Platt U. A fast h_2o total column density product from GOME validation with in-situ aircraft measurements. Atmos Chem Phys 2003;3(3):651–63. doi:10.5194/acp-3-651-2003. https://www.atmos-chem-phys.net/3/651/2003/.

[271] Walrafen GE. Raman spectral studies of the effects of temperature on water structure. J Chem Phys 1967;47(1):114–26. doi:10.1063/1.1711834.

[272] Wang H, González Abad G, Liu X, Chance K. Validation and update of OMI total column water vapor product. Atmos Chem Phys 2016;16(17):11379–93. doi:10.5194/acp-16-11379-2016. https://www.atmos-chem-phys.net/16/11379/2016/.

[273] Wang H, Liu X, Chance K, González Abad G, Chan Miller C. Water vapor retrieval from OMI visible spectra. Atmos Meas Tech 2014;7(6):1901–13. doi:10.5194/amt-7-1901-2014. https://www.atmos-meas-tech.net/7/1901/2014/.

[274] Wang J, Zhang L, Dai A, Van Hove T, Van Baelen J. A near-global, 2-hourly data set of atmospheric precipitable water from ground-based GPS measurements. J Geophys Res Atmos 2007;112(D11). doi:10.1029/2006JD007529. https://agupubs.onlinelibrary.wiley.com/doi/abs/10.1029/2006JD007529.

[275] Wang S, Streets DG, Zhang Q, He K, Kang DCS, Lu Z, et al. Satellite detection and model verification of NO_x emissions from power plants in northern China. Environ Res Lett 2010;5(4):044007. doi:10.1088/1748-9326/5/4/044007.

[276] Wang S, Zhang Q, Martin RV, Philip S, Liu F, Li M, et al. Satellite measurements oversee China's sulfur dioxide emission reductions from coal-fired power plants. Environ Res Lett 2015;10(11):114015. doi:10.1088/1748-9326/10/11/114015. http://stacks.iop.org/1748-9326/10/i=11/a=114015?key=crossref.12bf840455e95fc2cd51b5d496ef860f.

[277] Wang W, Flynn L, Zhang X, Wang Y, Wang Y, Jiang F, et al. Cross-calibration of the total ozone unit (TOU) with the ozone monitoring instrument (OMI) and SBUV/2 for environmental applications. IEEE Trans Geosci Remote Sens 2012;50(12):4943–55. doi:10.1109/TGRS.2012.2210902.

[278] Ware RH, Fulker DW, Stein SA, Anderson DN, Avery SK, Clark RD, et al. Suominet: a real-time national GPS network for atmospheric research and education. BAMS 2000;81(4):677–94. doi:10.1175/1520-0477(2000)081<0677:SARNGN>2.3.CO;2. https://doi.org/10.1175/1520-0477(2000)081〈0677:SARNGN〉2.3.CO;2.

[279] Weber M, Coldewey-Egbers M, Fioletov VE, Frith SM, Wild JD, Burrows JP, et al. Total ozone trends from 1979 to 2016 derived from five merged observational datasets – the emergence into ozone recovery. Atmos Chem Phys 2018;18(3):2097–117. doi:10.5194/acp-18-2097-2018. https://www.atmos-chem-phys.net/18/2097/2018/.

[280] Wellemeyer CG, Bhartia PK, Taylor S, Qin W. Version 8 Total Ozone Mapping Spectrometer (TOMS) algorithm. In: Proceedings of the XX quadrennial ozone symposium, 1–8 June, Kos, Greece, edited by C. Zerefos, Int. Ozone Comm., Athens., 1; 2004. p. 635–41.

[281] Wilmouth DM, Hanisco TF, Donahue NM, Anderson JG. Fourier transform ultraviolet spectroscopy of the $A^2\Pi_{3/2} \leftarrow X^2\Pi_{3/2}$ transition of bro. J Phys Chem A 1999;103(45):8935–45. doi:10.1021/jp991651o. https://doi.org/10.1021/jp991651o.

[282] Wittrock F, Richter A, Oetjen H, Burrows JP, Kanakidou M, Myriokefalitakis S, et al. Simultaneous global observations of glyoxal and formaldehyde from space. Geophys Res Lett 2006;33(16). doi:10.1029/2006GL026310. https://agupubs.onlinelibrary.wiley.com/doi/abs/10.1029/2006GL026310.

[283] World Health Organization. Ambient air pollution: a global assessment of exposure and burden of disease. Geneva, Switzerland: World Health Organization; 2016. https://www.who.int/phe/publications/air-pollution-global-assessment/en/.

[284] Wu Y-H, Key R, Sander S, Blavier J-F, Rider D. A panchromatic imaging fourier transform spectrometer for the NASA geostationary coastal and air pollution events mission. ProcSPIE 2011;8150:81500O. doi:10.1117/12.892437.

[285] Yang K, Carn SA, Ge C, Wang J, Dickerson RR. Advancing measurements of tropospheric NO_2 from space: new algorithm and first global results from OMPS. Geophys Res Lett 2014;41:4777–86. doi:10.1002/2014GL060136. https://agupubs.onlinelibrary.wiley.com/doi/abs/10.1002/2014GL060136.

[286] Yang K, Dickerson RR, Carn SA, Ge C, Wang J. First observations of SO2 from the satellite suomi NPP OMPS: widespread air pollution events over china. Geophys Res Lett 2013;40(18):4957–62. doi:10.1002/grl.50952. http://doi.wiley.com/10.1002/grl.50952.

[287] Yang K, Krotkov NA, Krueger AJ, Carn SA, Bhartia PK, Levelt PF. Retrieval of large volcanic SO_2 columns from the aura ozone monitoring instrument: comparison and limitations. J Geophys Res Atmos 2007;112(D24). doi:10.1029/2007JD008825. https://agupubs.onlinelibrary.wiley.com/doi/abs/10.1029/2007JD008825.

[288] Yang K, Krotkov Na, Krueger AJ, Carn Sa, Bhartia PK, Levelt PF. Improving retrieval of volcanic sulfur dioxide from backscattered UV satellite observations. Geophys Res Lett 2009;36(3):L03102. doi:10.1029/2008GL036036. https://agupubs.onlinelibrary.wiley.com/doi/abs/10.1029/2008GL036036.

[289] Yang K, Liu X, Bhartia P, Krotkov N. Direct retrieval of sulfur dioxide amount and altitude from spaceborne hyperspectral UV measurements: theory and application. J Geophys Res 2010;115:1–15. doi:10.1029/2010JD013982. http://so2.gsfc.nasa.gov/pdfs/Yang_KAsatochi_2010JD013982.pdf.

[290] Yang K, Liu X, Krotkov Na, Krueger AJ, Carn Sa. Estimating the altitude of volcanic sulfur dioxide plumes from space borne hyper-spectral UV measurements. Geophys Res Lett 2009;36(10):L10803. doi:10.1029/2009GL038025. http://www.agu.org/pubs/crossref/2009/2009GL038025.shtml.

[291] Zara M, Boersma KF, De Smedt I, Richter A, Peters E, Van Geffen JHGM, et al. Improved slant column density retrieval of nitrogen dioxide and formaldehyde for OMI and GOME-2A from QA4ECV: intercomparison, uncertainty characterization, and trends. Atmos Meas Tech 2018;2018:1–47. doi:10.5194/amt-11-4033-2018. https://www.atmos-meas-tech.net/11/4033/2018/.

[292] Zhang C, Liu C, Wang Y, Si F, Zhou H, Zhao M, et al. Preflight evaluation of the performance of the chinese environmental trace gas monitoring instrument (EMI) by spectral analyses of nitrogen dioxide. IEEE Trans Geosci Remote Sens 2018;56(6):3323–32. doi:10.1109/TGRS.2018.2798038.

[293] Zhang L, Jacob DJ, Boersma KF, Jaffe DA, Olson JR, Bowman KW, et al. Transpacific transport of ozone pollution and the effect of recent asian emission increases on air quality in North America: an integrated analysis using satellite, aircraft, ozonesonde, and surface observations. Atmos Chem Phys 2008;8(20):6117–36. doi:10.5194/acp-8-6117-2008. https://www.atmos-chem-phys.net/8/6117/2008/.

[294] Zhang L, Jacob DJ, Liu X, Logan JA, Chance K, Eldering A, et al. Intercomparison methods for satellite measurements of atmospheric composition: application to tropospheric ozone from TES and OMI. Atmos Chem Phys 2010;10(10):4725–39. doi:10.5194/acp-10-4725-2010. https://www.atmos-chem-phys.net/10/4725/2010/.

[295] Zhang Q, Streets DG, Carmichael GR, He K, Huo H, Kannari A, et al. Asian emissions in 2006 for the NASA INTEX-B mission. Atmos Chem Phys 2009;9:5131–53. doi:10.5194/acp-9-5131-2009. https://www.atmos-chem-phys.net/9/5131/2009/.

[296] Zhang Y, Li C, Krotkov NA, Joiner J, Fioletov V, Mclinden C. Continuation of long-term global SO_2 pollution monitoring from OMI to OMPS. Atmos Meas Tech 2017;10:1495–509. doi:10.5194/amt-10-1495-2017. https://www.atmos-meas-tech.net/10/1495/2017/.

[297] Zhong L, Louie PKK, Zheng J, Yuan Z, Yue D, Ho JWK, et al. Science-policy interplay: air quality management in the pearl river delta region and hong kong. Atmos Environ 2013;76:3–10. doi:10.1016/j.atmosenv.2013.03.012. http://www.sciencedirect.com/science/article/pii/S1352231013001787.

[298] Zhu L, Jacob DJ, Kim PS, Fisher JA, Yu K, Travis KR, et al. Observing atmospheric formaldehyde (HCHO) from space: validation and intercomparison of six retrievals from four satellites (OMI, GOME2a, GOME2b, OMPS) with SEAC4RS aircraft observations over the southeast US. Atmos Chem Phys 2016;16(21):13477–90. doi:10.5194/acp-16-13477-2016. https://www.atmos-chem-phys.net/16/13477/2016/.

[299] Zhu L, Jacob DJ, Mickley LJ, Marais EA, Cohan DS, Yoshida Y, et al. Anthropogenic emissions of highly reactive volatile organic compounds in eastern texas inferred from oversampling of satellite (OMI) measurements of HCHO

G. Gonzalez Abad, A.H. Souri and J. Bak et al. / Journal of Quantitative Spectroscopy & Radiative Transfer 238 (2019) 106478

23

columns. Environ Res Lett 2014;9(11):114004. doi:10.1088/1748-9326/9/11/114004. http://stacks.iop.org/1748-9326/9/i=11/a=114004.

[300] Zhu L, Mickley LJ, Jacob DJ, Marais EA, Sheng J, Hu L, et al. Long-term (2005–2014) trends in formaldehyde (HCHO) columns across North America as seen by the OMI satellite instrument: evidence of changing emissions of volatile organic compounds. Geophys Res Lett 2017;44(13):7079–86. doi:10.1002/2017GL073859. https://agupubs.onlinelibrary.wiley.com/doi/abs/10.1002/2017GL073859.

[301] Ziemke JR, Chandra S, Bhartia PK. Two new methods for deriving tropospheric column ozone from toms measurements: assimilated uars mls/haloe and convective-cloud differential techniques. J Geophys Res Atmos 1998;103(D17):22115–27. doi:10.1029/98JD01567. https://agupubs.onlinelibrary.wiley.com/doi/abs/10.1029/98JD01567.

[302] Ziemke JR, Chandra S, Duncan BN, Froidevaux L, Bhartia PK, Levelt PF, et al. Tropospheric ozone determined from aura OMI and MLS: evaluation of measurements and comparison with the global modeling initiative's chemical transport model. J Geophys Res Atmos 2006;111(D19). doi:10.1029/2006JD007089. https://agupubs.onlinelibrary.wiley.com/doi/abs/10.1029/2006JD007089.

[303] Zoogman P, Liu X, Suleiman RM, Pennington WF, Flittner DE, Al-Saadi JA, et al. Tropospheric emissions: monitoring of pollution (TEMPO). J Quant Spectrosc Radiat Transf 2017;186:17–39. doi:10.1016/j.jqsrt.2016.05.008. http://www.sciencedirect.com/science/article/pii/S0022407316300863.